Internal kinematics of giant H II regions in M101 with the Keck Cosmic Web Imager

Fabio Bresolin[1]*, Luca Rizzi[2], I-Ting Ho[3], Roberto Terlevich[4,5],
Elena Terlevich[4], Eduardo Telles[6], Ricardo Chávez[7],
Spyros Basilakos[8,9] and Manolis Plionis[8,10]

[1] *Institute for Astronomy, 2680 Woodlawn Drive, Honolulu, HI 96822, USA*
[2] *W.M. Keck Observatory, 65-1120 Mamalahoa Highway, Kamuela, HI 96743, USA*
[3] *Max Planck Institut für Astronomie, Königstuhl 17, 69117 Heidelberg, Germany*
[4] *Instituto Nacional de Astrofiísica Óptica y Electrónica, AP 51 y 216, 72000, Puebla, México*
[5] *Institute of Astronomy, University of Cambridge, Madingley Road, Cambridge CB3 0HA, UK*
[6] *Observatorio Nacional, Rua José Cristino 77, 20921-400 Rio de Janeiro, Brasil*
[7] *CONACYT-Instituto de Radioastronomía y Astrofísica, UNAM, Campus Morelia, C.P. 58089, Morelia, México*
[8] *National Observatory of Athens, P.Pendeli 15236, Athens, Greece*
[9] *Physics Department, Aristotle University of Thessaloniki, Thessaloniki 54124, Greece*
[10] *Academy of Athens Research Center for Astronomy & Applied Mathematics, Soranou Efessiou 4, Athens 11-527, Greece*

22 May 2020

ABSTRACT

We study the kinematics of the giant H II regions NGC 5455 and NGC 5471 located in the galaxy M101, using integral field observations that include the Hβ and [O III] $\lambda5007$ emission lines, obtained with the Keck Cosmic Web Imager. We analyse the line profiles using both single and multiple Gaussian curves, gathering evidence for the presence of several expanding shells and moving filaments. The line decomposition shows that a broad ($\sigma \simeq 30-50$ km s^{-1}) underlying component is ubiquitous, extending across hundreds of pc, while a large fraction of the narrow components have subsonic line widths. The supersonic turbulence inferred from the global line profiles is consistent with the velocity dispersion of the individual narrow components, i.e. the global profiles likely arise from the combined contribution of discrete gas clouds. We confirm the presence of very extended ($400-1200$ km s^{-1}) low-intensity line components in three bright star-forming cores in NGC 5471, possibly representing kinematic signatures of supernova remnants. For one of these, the known supernova remnant host NGC 5471 B, we find a significantly reduced [O III]/Hβ line ratio relative to the surrounding photoionized gas, due to the presence of a radiative shock at low metallicity. We explore the systematic width discrepancy between H I and [O III] lines, present in both global and individual spaxel spectra. We argue that the resolution of this long-standing problem lies in the physics of the line-emitting gas rather than in the smearing effects induced by the different thermal widths.

Key words: galaxies: individual: M101 – galaxies: ISM – ISM: kinematics and dynamics – H II regions.

1 INTRODUCTION

The supersonic stirring of the gas in giant H II regions, first inferred from the integrated line widths of the most luminous ionized nebulae in the galaxies M33 and M101 by Smith & Weedman (1970), remains a poorly explored and understood phenomenon. Some of the mechanisms put forward to inter-

pret the presence of these supersonic motions (including hydrodynamic turbulence and champagne flows) have not survived deeper scrutiny (Melnick et al. 1987; Yang et al. 1996). However, a dispute has persisted in the literature concerning the role of two alternative processes, namely self gravity (Terlevich & Melnick 1981; Tenorio-Tagle et al. 1993) and the energetics of massive stars (Gallagher & Hunter 1983; Chu & Kennicutt 1994). Our motivation for a new work on this subject is that a better understanding of supersonic

* E-mail: bresolin@ifa.hawaii.edu

motions in giant H II regions is crucial in order to use these objects as extragalactic distance indicators via the relationship between their integrated emission line widths and luminosities (Chávez et al. 2014; Fernández Arenas et al. 2018; González-Morán et al. 2019).

Through spatially-resolved spectroscopy of the supergiant H II region NGC 604 in M33, Yang et al. (1996) and Muñoz-Tuñón et al. (1996) reached the conclusion that, once corrected for thermal motions, the supersonic line widths can be accounted for, in approximately equal proportions, by virial motions and stellar winds. The latter produce fast-moving gas filaments and expanding shells, leading to the broad wings observed in the integrated line profiles.

In our vicinity, 30 Doradus (30 Dor) in the Large Magellanic Cloud is the quintessential giant H II region. Its integrated line profile stems from the combined contribution of discrete, macroscopic components (shells, filaments and clouds), characterized by subsonic line widths, as shown by Chu & Kennicutt (1994) and Melnick et al. (1999). Melnick et al. (2019) have recently argued that the motion of these discrete components inside the gravitational potential of the whole star forming region originates the supersonic width of the integrated line core, while stellar winds are responsible for the extended line wings.

Testing a paradigm that accounts for the line profiles of giant H II regions by invoking both gravity and stellar winds is a difficult task when looking, by necessity, beyond 30 Dor, because of the dramatic loss in spatial resolution. We can partly compensate by targeting similar or, perhaps more interestingly, more luminous nebulae using two-dimensional spectroscopy that extends the kinematics coverage over larger areas than currently feasible in 30 Dor (0.15×0.15 kpc^2, Torres-Flores et al. 2013). In this paper we focus on the internal gas kinematics of two of the objects included in the work by Smith & Weedman (1970), NGC 5455 and NGC 5471. Both are significantly more luminous than 30 Dor (Kennicutt 1984).

Both NGC 5455 and NGC 5471 have been the focus of previous kinematic studies, carried out utilizing echelle spectrographs and Fabry-Perot interferometers (e.g. Smith & Weedman 1970; Melnick 1977; Hippelein 1986). Skillman & Balick (1984) discovered that the asymmetric line profiles they observed in the bright cores of the H II regions in their sample, which included NGC 5455 and NGC 5471, required a decomposition into both a broad and a narrow Gaussian components. Line splittings and asymmetric line profiles in giant H II regions were confirmed by subsequent studies (e.g. Chu & Kennicutt 1994; Sabalisck et al. 1995). Other authors focused on high-velocity gas motions and known or suspected supernova remnants (SNRs) in NGC 5471 (Chu & Kennicutt 1986, = CK86; Castañeda et al. 1990; Chen et al. 2002), finding evidence for broad profiles underlying brighter, narrow components.

The work by Muñoz-Tuñón et al. (1995) was among the pioneering efforts made to obtain two-dimensional spectroscopy of extragalactic H II regions, using a Fabry-Perot imaging spectrograph in order to follow the Hα line profile across a 1.1×1.1 arcmin^2 field in NGC 604, NGC 5461 and NGC 5471. These authors detected split line profiles in low surface brightness portions of NGC 5471, and measured supersonic gas motions throughout the extent of this object. Broader lines were measured for two specific knots of star

formation, one of which displayed a clearly non-Gaussian line profile. Our work expands on this study using improved sensitivity and spectral resolution, confirming some of the conclusions by Muñoz-Tuñón et al. (1995), but also finding significant deviations from their study once a multi-component line analysis is implemented.

Our paper is organized as follows: we present our integral field data in Sect. 2, and global gas and line profiles in Sec. 3. We analyse the line profiles at each spaxel using single Gaussian fits and multiple Gaussian components in Sec. 4 and 5, respectively. In Sect. 6 we interpret the global supersonic line profiles, based on the results obtained from the multiple Gaussian fits. Sect. 7 focuses on the supernova remnant in NGC 5471 B. We consider the long-standing problem of the line width discrepancy between recombination and collisionally excited lines in Sect. 8. We conclude in Sect. 9 with a summary of our results.

2   OBSERVATIONS AND DATA REDUCTION

We observed the giant H II regions NGC 5455 and NGC 5471 in the galaxy M101 with the Keck Cosmic Web Imager (KCWI) integral field spectrograph (Morrissey et al. 2018) on the night of Feb 9, 2018. With the selected slicer configuration ($0''.35$ slice width) the field of view of the instrument is 8.4×20.4 arcsec^2. Three overlapping tiles observed contiguously yielded a total coverage of 21.4×20.4 arcsec^2 with a scale of 0.146 arcsec pixel^{-1}.

With the BH3 grating utilized for the observations the resulting spectra have a FWHM resolution of 0.30 Å, as measured from arc calibration frames, corresponding to a FWHM velocity resolution of 18.0 km s^{-1} at 5007 Å ($R \simeq 16,700$). The Gaussian instrumental broadening is therefore $\sigma_{instr} = 7.6$ km s^{-1}. A grating central wavelength of 4900 Å allowed us to fit simultaneously the Hβ, [O III] $\lambda 4959$ and [O III] $\lambda 5007$ nebular lines within the wavelength range covered on the detector ($4585 - 5195$ Å).

We obtained sequences of 300 s and 900 s exposures for NGC 5455, and 180 s for the brighter NGC 5471. Since the image quality varied substantially between different frames, we decided to retain for our analysis only the best-seeing (~ 1 arcsec[1]) data. Consequently, the total exposure time per single tile amounts to 900 s in the case of NGC 5455 and 360 s in the case of NGC 5471. Despite the short integrations, the [O III] $\lambda 5007$ line saturates in a few pixels of the brightest region of NGC 5471. In our line profile analysis we therefore used the information derived from the [O III] $\lambda 4959$ line for these pixels.

Using the data reduction pipeline (described by Morrissey et al. 2018) we produced geometrically corrected, wavelength calibrated data cubes that account for the effects of differential atmospheric refraction. We then mosaicked and combined the three tiles obtained for each H II region with the DPUSER[2] software (Ott 2012) and IRAF[3] routines.

---

[1] 1 arcsec = 33 pc at an adopted distance of 6.8 Mpc (Fernández Arenas et al. 2018).

[2] http://www.mpe.mpg.de/~ott/dpuser.

[3] IRAF is distributed by the National Optical Astronomy Observatories, which are operated by the Association of Universities for
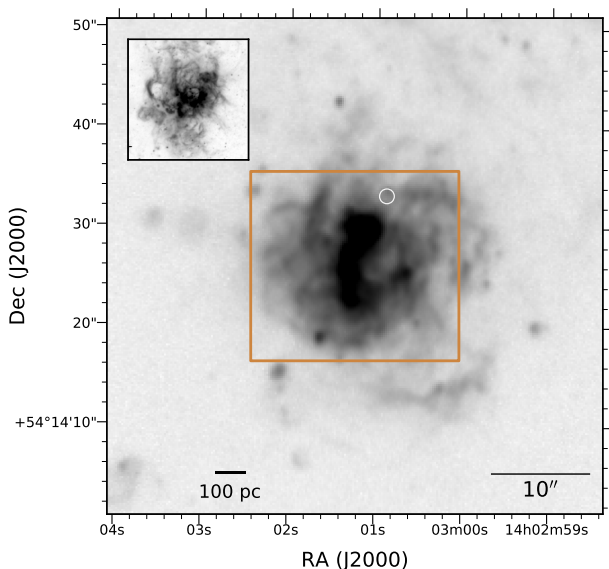
Figure 1. Hα image of NGC 5455 (extracted from the CFHT Science Archive) with overlay of the field observed with KCWI (rectangle). In the inset at the upper left the giant H II region NGC 604 in the galaxy M33 is shown at the same physical scale, for comparison. The circle indicates the position of SN 1970G (Dittmann et al. 2014) for reference.
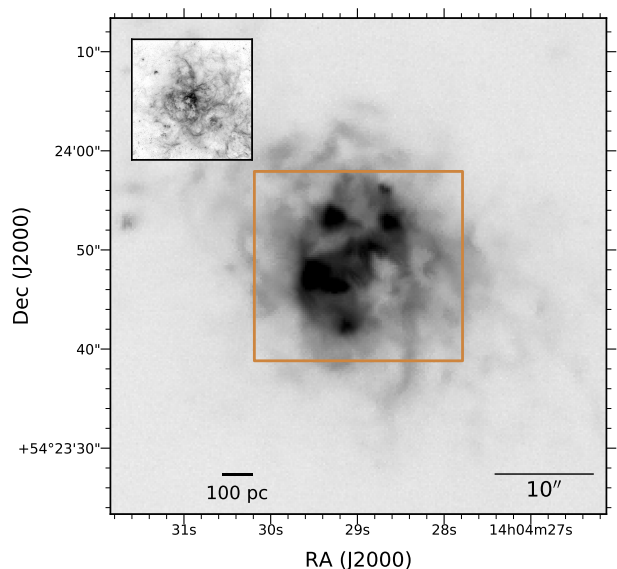
Figure 2. Hα image of NGC 5471 (extracted from the CFHT Science Archive) with overlay of the field observed with KCWI (rectangle). In the inset at the upper left the giant H II region 30 Dor in the LMC is shown at the same physical scale, for comparison (image from the ESO archive).

In order to facilitate the subsequent analysis we spatially rebinned the images by a factor of three (1 pixel = 0.44 arcsec). Fig. 1 and 2 display narrow-band Hα images of NGC 5455 and NGC 5471, respectively, illustrating the spatial extent of the data cubes. It can be seen that the KWCI data fully cover the bright portion of the star forming region in both cases, extending over ∼0.69 × 0.63 kpc^2 with a spatial resolution of ∼30 pc, and excluding only relatively faint outlying gaseous filaments.

## 3 GLOBAL GAS PROPERTIES AND LINE PROFILES

The KCWI data cubes were handled with the `spectral-cube` package, which is part of the Astropy Project (Astropy Collaboration et al. 2013, 2018). As a first step, in order to visualize the spatial distribution of the gas emission properties in the two H II regions, we produced continuum-subtracted narrow-band images corresponding to the Hβ and [O III] line emission. In Fig. 3 (for NGC 5455) and 4 (for NGC 5471) we show the Hβ line emission map (left panel) and the [O III] λ5007/Hβ line ratio map (right panel) thus obtained. In these images, as in all other images and maps presented in this paper, North is at the top and East to the left.

In the case of NGC 5455 (Fig. 3) we have labelled as 'A' the single, bright blob in the northern section of the nebula. Although this is not obvious because of the stretch used to display the map, region A dominates the overall line emission of NGC 5455. The gas excitation, measured by the

[O III]/Hβ line ratio (right panel of Fig. 3), peaks at the position of blob A, but its spatial distribution does not fully correlate with that of the Hβ flux in the remaining parts of the nebula.

NGC 5471 is a giant H II region containing multiple ionizing clusters. In the left panel of Fig. 4 we have identified the five positions (A through E) defined by Skillman (1985), where A corresponds to the brightest star-forming knot in the region – comparable in luminosity and ionizing cluster mass to 30 Dor (Chen et al. 2005) – while B hosts a SNR, identified from optical excitation and nonthermal radio emission properties (Skillman 1985) and characterized by broad emission lines (CK86, Chen et al. 2002 – the latter authors favour the notion of a hypernova remnant). The labeling of the object immediately to the west of A as A′ follows Muñoz-Tuñón et al. (1995).

While the gas excitation is high throughout most of the extent of NGC 5471, and in general where the Hβ emission peaks, as seen in the right panel of Fig. 4, there are regions of localized lower excitation, corresponding with the three shells identified by Chen et al. (2002) on the basis of enhanced [S II]/Hα line emission, the classic optical signature for the presence of a radiative shock (Mathewson & Clarke 1973). One of these ('s1' in Fig. 4) is associated with knot B and its SNR. Chen et al. (2002) suggested that also the remaining two shells are related to the presence of SNRs. [O III]-to-Balmer line ratios that are low in comparison to nearby photoionized gas have been presented for SNRs before (see Shull 1983 for objects in the LMC). The explanation for the significant drop in the [O III] λ5007/Hβ line ratio seen in Fig. 4 in correspondence of shocked gas regions lies in the low metallicity of NGC 5471, 12 + log(O/H) ≃ 8.05 (Kennicutt et al. 2003), equalling that of the Small Magellanic Cloud. At this metallicity the [O III] λ5007/Hβ ratio predicted by shock models can be significantly lower than for
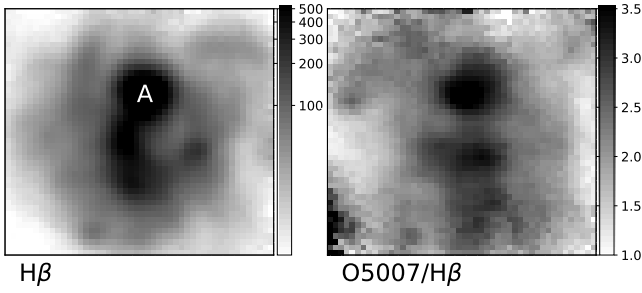
Figure 3. (Left) Continuum-subtracted Hβ image of NGC 5455 derived from the KCWI data cube. The spot with the brightest emission is labelled as A. (Right) The [O III] $\lambda5007$/Hβ emission line ratio image. In this and subsequent figures we refer to [O III] $\lambda5007$ as O5007.
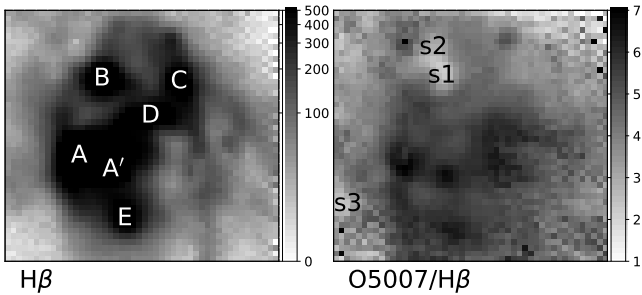
Figure 4. (Left) Continuum-subtracted Hβ image of NGC 5471 derived from the KCWI data cube. The letters A – E refer to the emission peaks identified by Skillman (1985), while A′ follows from Muñoz-Tuñón et al. (1995). (Right) The [O III] $\lambda5007$/Hβ emission line ratio image. The three shells identified by Chen et al. (2002) are labelled as s1, s2 and s3.

photoionized gas (e.g. compare Fig. 21 of Allen et al. 2008 with the H II region diagnostic diagram shown in Fig. 4 by Bresolin et al. 2012).

In Fig. 5 and 6 we present high spatial resolution colour composite images of NGC 5455 and NGC 5471, respectively, that we obtained from *Hubble Space Telescope* (*HST*) archival data (Programs IDs 14678 and 6829 – for colour images of NGC 5471 see also Chen et al. 2002, 2005). The detailed morphological information they provide is helpful to interpret the kinematical data presented in the following sections. The color-magnitude analysis based on the NGC 5471 *HST* data by García-Benito et al. (2011) indicates that the star formation activity has proceeded at a nearly constant rate during the past ∼100 Myr over the extent of this giant H II region.

3.1   Global line profiles

In order to compare the widths of integrated line profiles obtained from our data with published values we simulated observations through a $2'' \times 2''$ aperture, centred on knot A in both objects (see Fig. 3 – 4), and measured the FWHM of the Hβ and [O III] $\lambda5007$ lines from the extracted spectra, using Gaussian fits. We repeated the measurements with a $2'' \times 4''$ aperture, centred on the approximate geometrical centre of

the ionized gas distribution, and finally using the whole field of view. In the latter case the velocity dispersions, referring to a ∼0.7 kpc physical scale, can be directly compared to those obtained for poorly resolved systems (e.g. H II galaxies) viewed at large distances.

The observed velocity dispersion σ_{obs}, calculated as FWHM/2.355, was corrected for the effects of instrumental (σ_{instr}), thermal (σ_{th}) and fine structure (σ_{fs} – Hβ line only) broadening, according to:

$$\sigma = (\sigma_{obs}^2 - \sigma_{instr}^2 - \sigma_{th}^2 - \sigma_{fs}^2)^{1/2}. \quad (1)$$

We adopted $\sigma_{instr} = 7.6$ km s^{-1} (see Sec. 2) and σ_{fs} (Hβ) $= 2.4$ km s^{-1} from García-Díaz et al. (2008). The thermal component was evaluated, assuming a Maxwellian velocity distribution, as:

$$\sigma_{th} = \left(\frac{k \, T_e}{m} \right)^{1/2}, \quad (2)$$

where m is the mass of the ion (either H$^+$ or O^{++}). For the electron temperature we referred to the T([O III]) values published by Kennicutt et al. (2003), adopting $T_e = 10,000$ K for NGC 5455 (= H409 in their Table 2) and the average of four knots (A – D), $T_e = 13,275$ K, as representative for NGC 5471.

The results of this procedure are summarized in columns 3 ($2'' \times 2''$ aperture), 4 (geometrical center) and 5 (full field of view) of Table 1. Our comparison data are taken from Smith & Weedman (1970, = SW70, column 6), Hippelein (1986, = H86, column 7) and Fernández Arenas et al. (2018, = F18, column 8). We measure larger values of the velocity dispersion in NGC 5471 compared to NGC 5455, in agreement with H86, but in contrast with SW70 and F18. Our σ values for NGC 5455 are in good agreement with H86 if we consider the $2'' \times 2''$ aperture, but in the case of NGC 5471 we find agreement by selecting the other apertures. The line widths reported in Table 1 can be rather sensitive to the position chosen for the aperture center, both for our data and the published data, and we attribute the differences with published measurements to variations in aperture sizes and positions. As already observed by F18, such differences can amount to approximately 10%, consistent with our findings.

4   SINGLE LINE PROFILE FITS

In this section we look at the spatially resolved behaviour of the line profiles across NGC 5455 and NGC 5471, by fitting single Gaussians to the profiles of both Hβ and [O III] $\lambda5007$ in each spaxel. The line profiles of giant H II regions often deviate from simple Gaussian curves, displaying asymmetries, extended wings and multiple components, indicative of the complex kinematics resulting from the superposition of discrete broken filaments and expanding shells along the line of sight (Sabalisck et al. 1995; Yang et al. 1996). Numerous examples can be seen in Fig. 7 and 8, where we illustrate the variation of the [O III] $\lambda5007$ line profile across the KCWI field of view in NGC 5455 and NGC 5471, respectively (we selected the stronger [O III] $\lambda5007$ line in order to

Figure 5. Colour composite of NGC 5455, obtained from *HST* WFC3 images in the F438W (blue channel), F555W (green channel) and F600LP (red channel) filters. The field of view is equivalent to the KCWI data cube coverage, corresponding to 690×630 pc^2.

Figure 6. Colour composite of NGC 5471, obtained from *HST* WFPC2 images in the F547M (blue channel), F675W (green channel) and F656N (red channel) filters. The field of view is equivalent to the KCWI data cube coverage, corresponding to 690×630 pc^2.

Table 1. Line width comparison.

H II region	line	$2'' \times 2''$ aperture	$2'' \times 4''$ aperture	σ (km s^{-1}) full field of view	SW70	H86	F18
(1)	(2)	(3)	(4)	(5)	(6)	(7)	(8)
NGC 5455	Hβ	20.2 ± 0.4[1]	21.8 ± 0.4[3]	21.2 ± 0.3	23.9	20.6 ± 0.4	23.4 ± 1.1
	[O III]	17.8 ± 0.4[1]	21.4 ± 0.4[3]	19.5 ± 0.3	...	17.5 ± 0.3	...
NGC 5471	Hβ	24.2 ± 0.9[2]	19.6 ± 0.9[3]	22.7 ± 0.3	19.4	22.4 ± 0.4	20.0 ± 0.9
	[O III]	23.3 ± 0.9[2]	18.6 ± 0.9[3]	22.0 ± 0.3	...	19.5 ± 0.3	...

[1]Aperture centred on NGC 5455 A.   [2]Aperture centred on NGC 5471 A.   [3]Aperture centred on approximate geometrical centre of ionized gas distribution.
SW70: Smith & Weedman (1970, taking $T_e = 10^4$ K); H86: Hippelein (1986); F18: Fernández Arenas et al. (2018).

maximize the signal-to-noise ratio). However, a single Gaussian fitting approach keeps the line profile analysis easily tractable, at the same time providing important first-order information about the gas kinematics, via the determination of line width and velocity variations across nebulae. Fits to line profiles that are clearly split into at least two components are affected by large residuals, but still give insight into the presence of separate shells or filaments and their velocities (Muñoz-Tuñón et al. 1996). A multi-component analysis that further addresses this issue will be presented in the following section.

The line profiles in each resolution element of the re-binned data cubes were fitted with single Gaussian functions with the `lmfit` package (v. 0.9.13, Newville et al. 2019). For our analysis we retained lines whose peak is at least 10 times larger than the rms noise of the continuum, as a tradeoff between accuracy of the fit parameters and spatial coverage completeness. This criterion impacted low-flux regions along the edges of the field of view. The flux-weighted average cen-

troid velocity was adopted as the zero-point of the velocity scale. The yellow lines in Fig. 7 and 8 show examples of the Gaussian fits across both NGC 5455 and NGC 5471.

4.1 $I - \sigma$ diagrams

In two separate studies of the spatially resolved kinematics of the giant H II regions NGC 604 and NGC 588 in the nearby galaxy M33, Muñoz-Tuñón et al. (1996, = M96) and Yang et al. (1996, = Y96) correlated the peak intensity (I) of single Gaussian fits to strong nebular lines with either the velocity dispersion (σ) or the FWHM of the line profiles, respectively. The $I - \sigma$ diagram thus introduced represents a diagnostic tool that helps to differentiate emission line broadening mechanisms in giant H II regions, and its use has been extended to kinematical investigations of H II galaxies and other star-forming dwarf galaxies (Martínez-Delgado et al. 2007; Bordalo et al. 2009; Moiseev & Lozinskaya 2012). Based on the line widths they measured, both
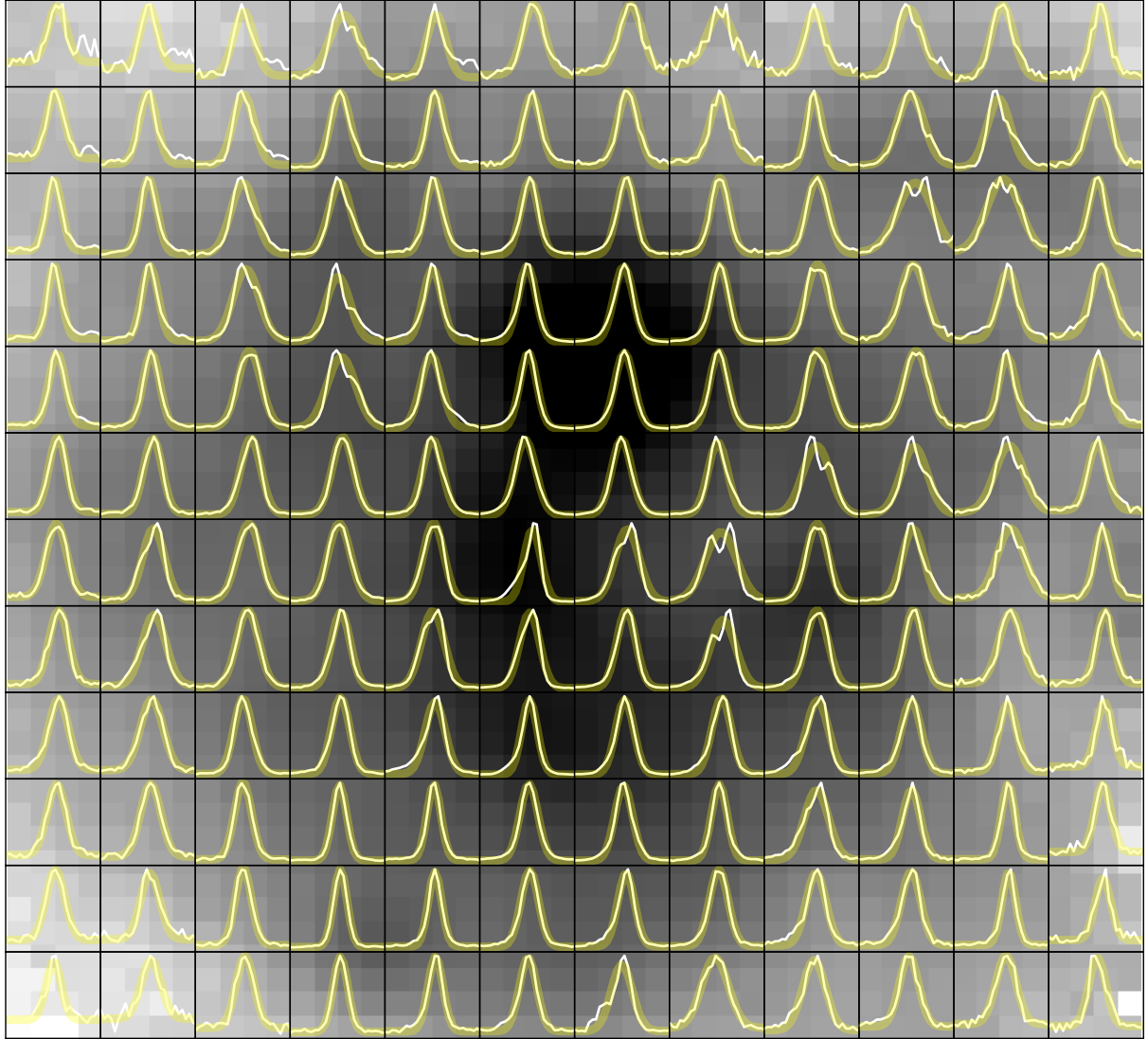
Figure 7. [O III] λ5007 line profiles (white lines) and Gaussian fits (yellow thick lines) in individual spatial resolution elements across the Hβ narrow-band image of NGC 5455. The spacing between elements is about 1.7 arcsec. In each subframe the radial velocity ranges between -120 and $+120$ km s^{-1}, where the zero point is determined from the spatially integrated spectrum of the nebula. There is a large variation of peak intensity between the subframes, with strong lines approximating Gaussian curves, while fainter lines often display more complex profiles.

M96 and Y96 concluded that the gas motions are supersonic[4] at most locations, but that the scatter in σ increases strongly towards lower line intensities. The highest σ values are encountered in the faintest nebular regions. Both papers associated the fainter and high-velocity dispersion regions with gas shell structures originating from the effects of stellar winds and SNRs, while concluding that virial motions are responsible for slower, but still supersonic, gas motions. A minimum ($\sigma \simeq 17$ km s^{-1}) value of the velocity dispersion was found for NGC 604, irrespective of line intensity, while in the case of NGC 588 a similar minimum could not be established, with a significant fraction of the nebular gas exhibiting subsonic σ values. This was interpreted as possibly

due to a more evolved kinematic state. M96 demonstrated how prominent shell structures define inclined bands in the $I - \sigma$ diagram, extending from low I and high σ locations (corresponding to the shell centers – the line width of the Gaussian fits measuring the maximum expansion velocity of the shells) to high I and low σ locations (at the shell edges).

In the bottom-left panels of Fig. 9 and 10 we display the $I - \sigma$ diagrams for NGC 5455 and NGC 5471, respectively, obtained from fits to the Hβ line (equivalent information is gathered from the [O III] λ5007 line). Instead of the peak intensity we have used the fitted line flux – this choice introduces no significant difference. In each figure we use colors in order to map different regions of the $I - \sigma$ diagram to the corresponding emitting location in the top left panel (where Hβ image isophotes are displayed). The error bars at the bottom represent the standard deviation of the difference $\sigma([\text{O III}]\lambda5007) - \sigma([\text{O III}]\lambda4959)$, an esti-

---

[4] The isothermal sound speed for an H II region at 10^4 K is $c_s \simeq$ 11 km s^{-1} (e.g. Spitzer 1968)
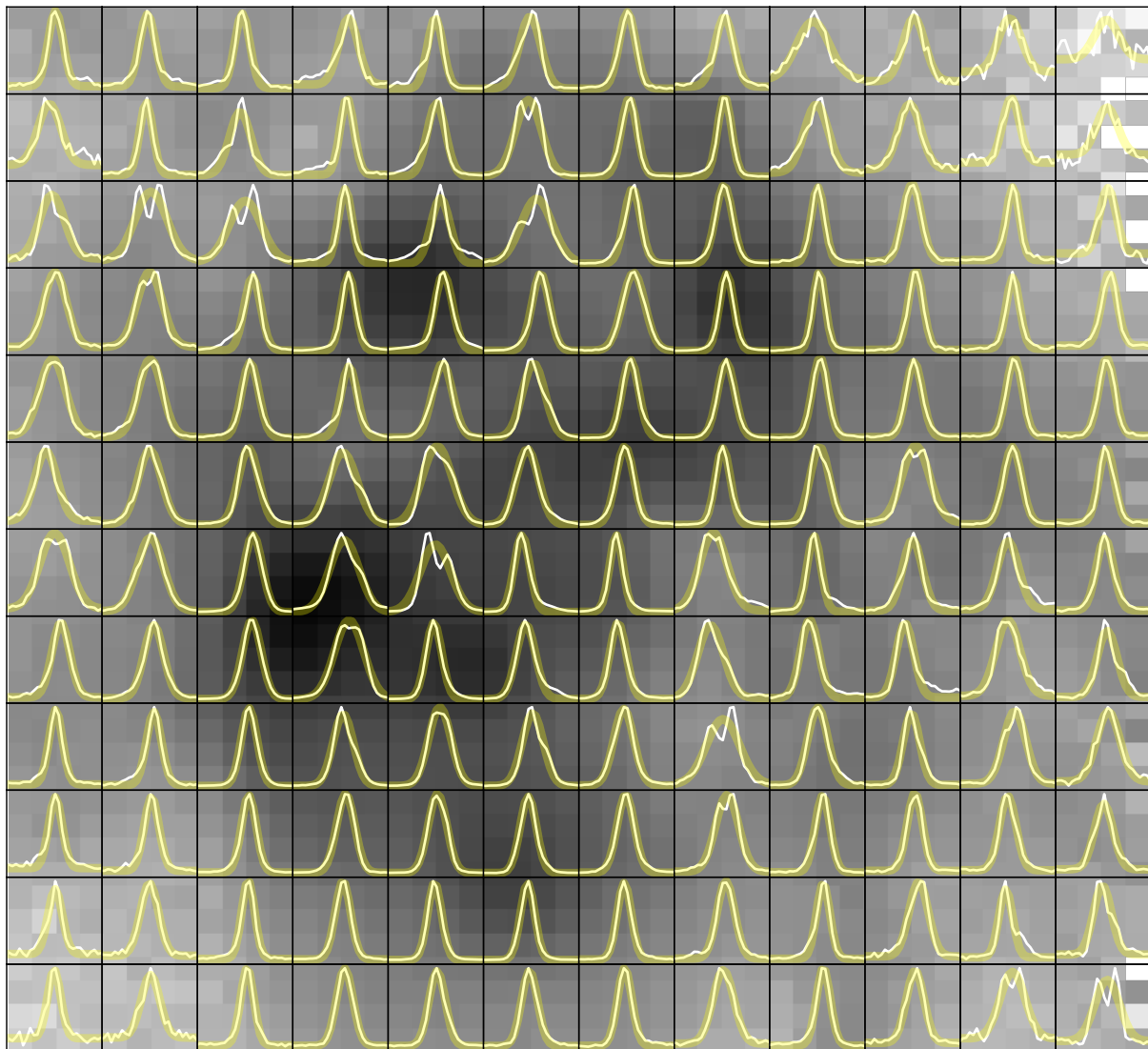
Figure 8. Same as Fig. 7, for NGC 5471.

mate of the uncertainty in σ, since the two lines have the same intrinsic width. Maps of the velocity dispersion σ are shown in the top right panels. Finally, the $V - \sigma$ diagrams in the bottom right panels display the velocity centroid of each Gaussian as a function of the velocity dispersion. The latter diagram tests whether portions of the nebulae possess streaming rather than random motions along the line of sight (see Martínez-Delgado et al. 2007; Bordalo et al. 2009). The two bottom diagrams include a horizontal line, drawn at the flux-weighted average σ value: 20.6 and 20.7 km s^{-1} for NGC 5455 and NGC 5471, respectively. These differ somewhat from those reported in column 5 of Table 1. This is due to the fact that in that case we used the full (unbinned) data cube information.

NGC 5455

The $I - \sigma$ diagram of NGC 5455 (Fig. 9, bottom left panel) appears qualitatively similar to the diagram presented for

NGC 588 by M96, where an approximately constant lower σ is *not* observed.

We have assigned different colors to various regions in this diagram, in order to identify (with corresponding colors in the top left panel) where the emission originates. The main emission knot (labelled 'A' – red color) defines the bright tip of the main horizontal band in the $I - \sigma$ diagram, with $\sigma \simeq 18 - 21$ km s^{-1}. The largest σ values in NGC 5455 are encountered in a slightly offset position from a weak filament labelled 'NW', and are represented in magenta. In contrast, a weak emission peak, labelled '2', corresponds to a region of low σ (in yellow), well confined in the $I - \sigma$ plot. The bright plume to the south of the main knot, labelled '1' (blue and cyan), displays a small range in velocity dispersion. The $V - \sigma$ diagram in the bottom right panel indicates a mild velocity gradient of $\sim$15 km s^{-1} across the plume, with the northern (southern) portion having negative (positive) velocities. Other regions of relatively large σ ($24 - 30$ km s^{-1} – green and pink) appear spatially well defined and immersed in diffuse gas characterized by a disper-
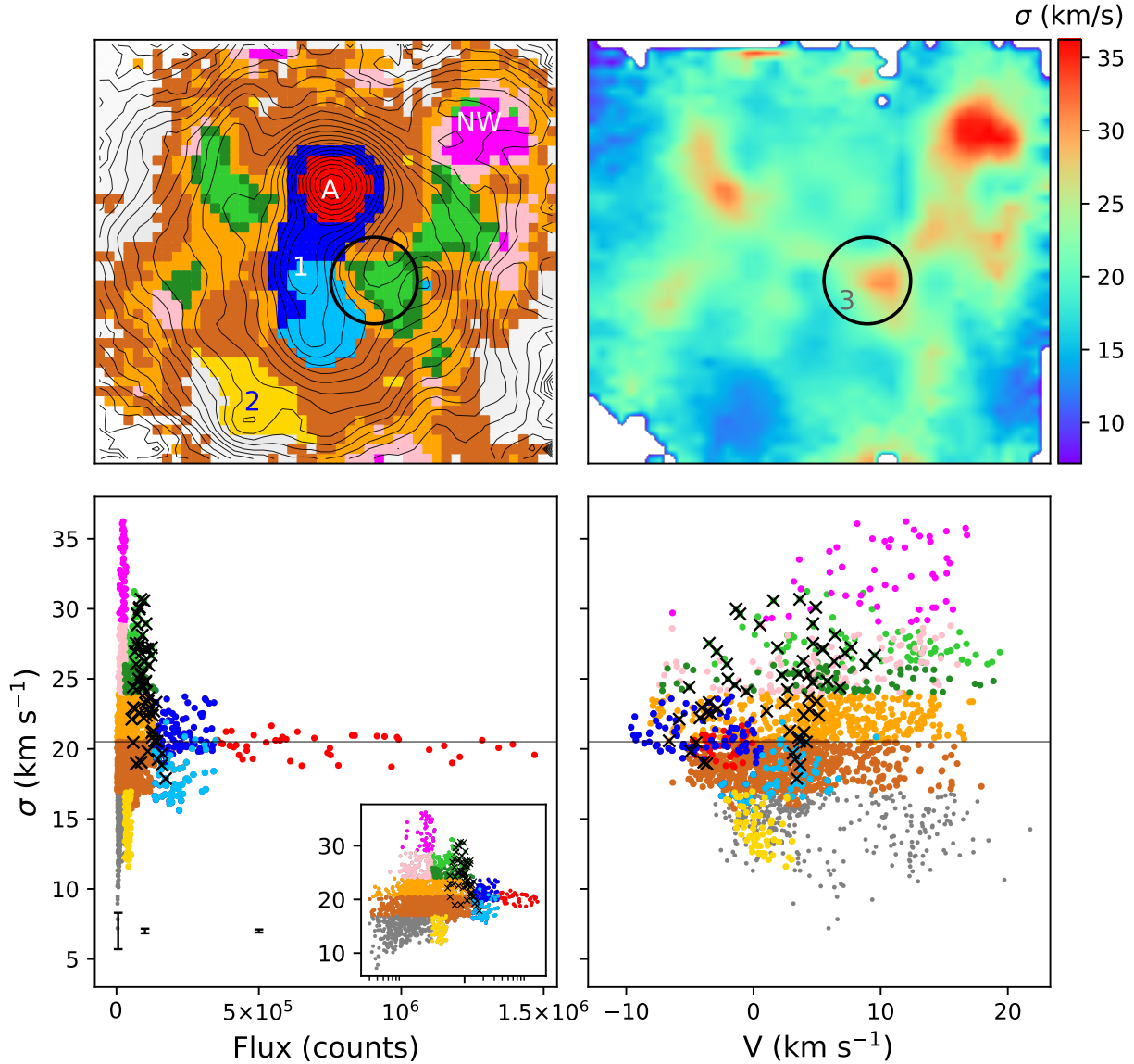
Figure 9. Results from single Gaussian fits for NGC 5455. (Top left): Isocontours of the Hβ flux distribution (arbitrary level spacing). The colored areas represent regions selected in the $I-\sigma$ diagram shown in the panel below. (Top right): velocity dispersion map, smoothed with a bilinear interpolation. (Bottom left): $I-\sigma$ diagram, where we use different colors to isolate portions that are mapped onto the top left panel. The error bars represent the uncertainties estimated by comparing the widths of the two [O III] lines, $\lambda4959$ and $\lambda5007$. The inset uses the logarithmic scale for the flux. (Bottom right): $V-\sigma$ diagram, using the same colour code. The horizontal line in the two bottom plots represents the flux-weighted average σ value. The circle in the top row identifies the location of slit profiles with a maximum in σ, that we associate with the presence of a shell.

sion similar to that of the brightest blob ($\sigma \sim 17-24$ km s^{-1} – orange and maroon). Knot A appears to be encircled by a high-σ network (in green). Towards the edges of the field of view the velocity dispersion falls below 15 km s^{-1} (in grey in the left panels), and some of the faintest points approach or fall below the isothermal sound speed.

The *HST* image of Fig. 5 shows a cavity ($\sim$100 pc in diameter) in the ionized gas distribution, immediately to the W of the bright plume, and centred on an ensemble of well-resolved bright stars. At this location we observe split line profiles (see Fig. 7) and find a peak in the σ map, identified by a circle labelled as '3' in Fig. 9 (top right). The Gaussian fits within this circle define an inclined band in the $I-\sigma$ diagram (black crosses in the bottom left panel). The as-

sociation of a visible shell structure with such an inclined band agrees with the findings of M96. If we interpret the maximum measured velocity dispersion ($\sim$30 km s^{-1}) as the velocity separation between receding and approaching sides of the shell along the line of sight, we obtain a dynamical age for this structure of 3.3 Myr.

Several arcs and filaments are present throughout the region covered by our KCWI observations. In particular what appears to be a faint, large broken shell, with a diameter of $\sim$160 pc, is barely visible in the NW corner of the *HST* image, matching the location where we measure the largest velocity dispersion ($\sim$35 km s^{-1}) in the NGC 5455 area. We derive a dynamical age of approximately 4.5 Myr, but, contrary to the smaller shell we have identified earlier,
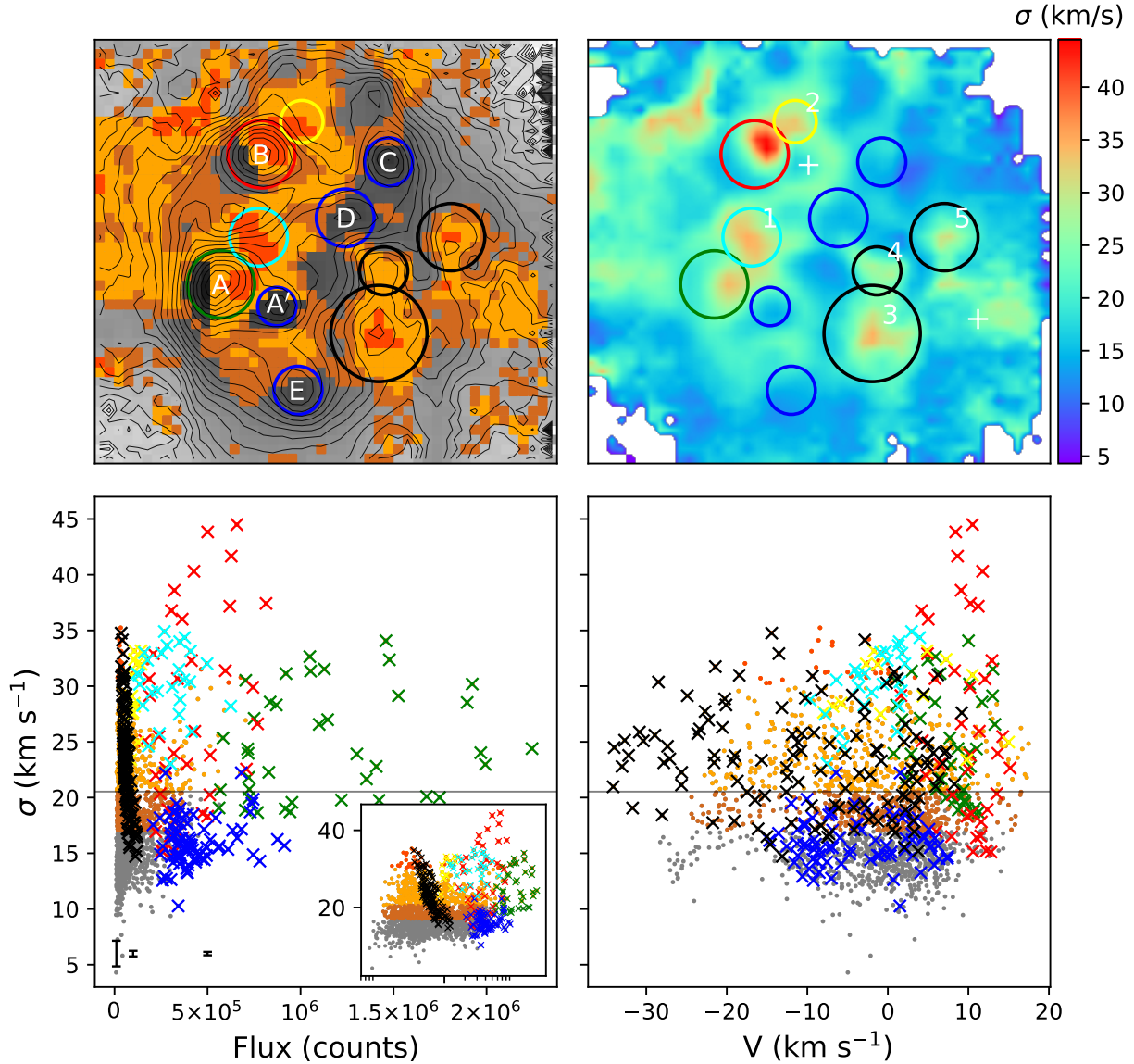
Figure 10. Same as Fig. 9, for NGC 5471. See text for the identification of the different features.

there is puzzlingly no prominent association of bright stars in this region: we cannot explain this localized large gas turbulence with the presence of massive stars. It is conceivable that we are observing a blowout region (Mac Low & McCray 1988; Tenorio-Tagle & Bodenheimer 1988) venting gas into the galactic halo.

NGC 5471

The case of NGC 5471, a multi-core giant H II region (Kennicutt 1984), appears more complex compared to NGC 5455. We can recognize several different features in the narrow band images, identified by circles in the top left panel of Fig. 10 (including the knots we labelled in Fig. 4). Points inside these circles are mapped onto the $I-\sigma$ diagram (bottom left panel) with crosses of the same color. The single, most striking feature of the diagram is that large values of the velocity dispersion are met throughout the intensity scale. In particular, the largest σ is measured in the luminous knot

B (red circle and crosses), where the σ range is also very high ($15-45$ km s^{-1}). These findings are largely due to the inadequacy of a single Gaussian fit for this object, as we will describe in Sect. 7. In fact, the line profile in this area (see Fig. 8) shows a faint, but very broad, component superposed on a stronger, narrow component, matching the profile shape presented by CK86. The σ map in the top right panel shows that it is the NW sector of the area encircled for knot B that is characterized by a high velocity dispersion, up to ~ 45 km s^{-1}. This roughly agrees with the location where a large [S II]/Hα line ratio is found in the *HST* imaging presented by Chen et al. (2002), and associated with the SNR shock region. Further details will be presented in Sect. 7.

The velocity dispersion is high ($20-35$ km s^{-1}) also in knots A (green), and in two small regions to the NW of both knot A ('1' – cyan) ad knot B ('2' – yellow), labelled in the top right panel for clarity. We note that also in the case of knot A, as in knot B, the highest σ values are confined to a small area to the W of the knot center. Interestingly, the

other knots (A′, C, D and E), are characterized by *low* velocity dispersion values $\sigma < \sigma_0$, where $\sigma_0 = 20.7$ km s^{-1} is the flux-weighted average velocity dispersion. We have represented them using the same blue color, because of the similar location they occupy in the $I - \sigma$ diagram, although the $V - \sigma$ plot (bottom right) shows a range of radial velocities.

We display in orange (red) the remaining points with $\sigma_0 < \sigma < 30$ (> 30) km s^{-1}. The low-σ knots (from E in the south to C in the north) are located in a low-σ ring-like structure surrounding knots A and B, that roughly matches the edges of the elongated ovoidal bubble easily recognizable in narrow-band images (Fig. 4). We speculate that we might be observing a rough σ-cluster age relation in this giant H II region. The *HST* data analysis by García-Benito et al. (2011) led to an estimated age of 3 ± 2 Myr for the ionizing cluster in knot A, and 5 ± 2 for the clusters in knots A′, B, C, D and E, although the authors caution about the results for the fainter objects (C, E). Moreover, for two clusters whose position is indicated by crosses in the top right panel García-Benito et al. (2011) derive an even older age of 9 ± 3 Myr, while the velocity dispersion in this area is around 20 km s^{-1}. There is thus some circumstantial evidence that a young cluster (A) is associated with higher-than-average velocity dispersion, while for older clusters σ falls back to average or below-average values.

To the west lies a region where the velocity dispersion rises again, and where we identified three possible expanding shells, indicated by black circles and labelled with numbers 3, 4 and 5. The points in these areas define an inclined band in the $I - \sigma$ diagram, the signature of shell structures in the interpretation given by Muñoz-Tuñón et al. (1996). The spaxels contained within the three putative shells span a wide range in velocity centroid (-30 to 10 km s^{-1} – see bottom right panel). These structures correspond to roughly circular 'clearings' in the ionized gas distribution in the *HST* image of Fig. 6. The largest one ('3', $\sim$70 pc in radius), following the same interpretation of an expanding shell as done before, yields a kinematic age of $\sim$4 Myr.

4.2   The radial velocity field

In Fig. 11 we display maps of the velocity centroids for our two targets, determined from single Gaussian fits to the [O III] $\lambda5007$ line (we remind the reader that the velocity zero point is defined by the flux-weighted average velocity). The radial velocity range in NGC 5471 is $\sim$60% higher than in NGC 5455, indicative of the larger gas motions in the higher luminosity, multi-core nebula. We ascribe the morphology of these maps to the filamentary distribution of the ionized gas and the presence of expanding shells. Different filaments or 'voids' that we can identify in the *HST* images can be matched with features in the velocity field. For example, the significant radial velocity gradient ($\Delta V \simeq 30$ km s^{-1}) we observe in the NW region of NGC 5455 develops across the broken bubble we described earlier, with filaments at the top approaching us at 10-12 km s^{-1}, those near the bottom receding at 15-18 km s^{-1}. This is also the location with the highest σ in Fig. 9. The arc of negative velocity immediately to the SE of knot A corresponds to a transition band of lower stellar density identifiable in the *HST* image (Fig. 5) between knot A and the bright stellar clusters to its south. For NGC 5471 we can associate the largest approaching ra-
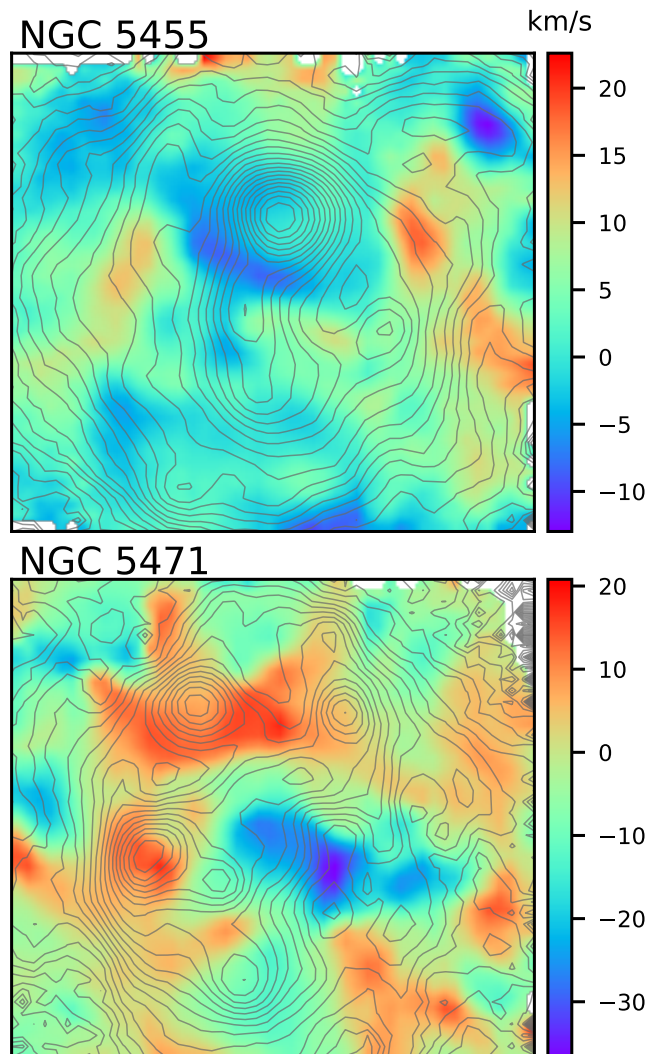
Figure 11. Radial velocity field in NGC 5455 (top) and NGC 5471 (bottom) from single Gaussian fits to the [O III] $\lambda5007$ line. In this and subsequent plots we include arbitrarily spaced isophotes of the Hβ emission, for reference.

dial velocity with the intersecting region between shells 3 and 4 (se Fig. 10 for identification). The gas in the 'shell area' is generally characterized by negative velocities (i.e. approaching the observer), while the gas surrounding knots A and B moves at the highest receding velocity.

5   MULTIPLE LINE PROFILE FITS

The emission line profiles of nearby giant H II regions and blue compact galaxies often deviate from single Gaussians, and multiple narrow subcomponents are revealed at high spectral resolution (Chu & Kennicutt 1994; Melnick et al. 1999; Bordalo & Telles 2011; Chávez et al. 2014). In addition, a relatively low spectral resolution is sufficient to uncover a broad underlying component (Méndez & Esteban 1997; Firpo et al. 2011; Hägele et al. 2013), from which expansion velocities of several hundred km s^{-1} are inferred, although extreme values of thousands of km s^{-1} have also

been measured (e.g. Castañeda et al. 1990; Roy et al. 1992). A broad underlying component is also observed in non-giant H II regions (see Castañeda 1988 for the case of the Orion nebula).

Multiple Gaussian fits were calculated for each spaxel of our KCWI data using `lmfit` (Newville et al. 2019), allowing a number of components up to $N_{comp} = 8$, if statistically justified. This decision was based on the Bayesian information criterion (BIC – Schwarz 1978), which is widely used in astrophysics for model selection (Liddle 2004). We preferred the BIC over the Akaike information criterion (Akaike 1974), also calculated by `lmfit`, because it is more conservative in the number of model parameters (in our case the number of Gaussians to include). We followed guidelines from Kass & Raftery (1995, see also Liddle 2007 or Shi et al. 2012 for astronomy-related examples) in adopting a minimum decrease $\Delta BIC = -10$ to justify the inclusion of an additional Gaussian component in our model profiles.

In the case of [O III] $\lambda 5007$, the strongest line in our data, the majority of our fits (about 3/4 of the spaxels) are characterized by $2 \leqslant N_{comp} \leqslant 4$. We experimented with forcing the weaker Hβ lines to have the same number of components at the same wavelengths as the [O III] $\lambda 5007$ lines, allowing for different widths and intensities. We found that this procedure works in some cases, but more often the comparison of the decomposition of the two line profiles is less than satisfactory – the significantly larger thermal broadening of the Balmer lines is the culprit. The different amounts of thermal broadening explains why at the very high spectral resolution ($R \sim 10^5$) used by Melnick et al. (2019) the [O III] lines are resolved into a larger number of components than Hβ. Besides, trying to match the components in the two lines worsens the fit to the Hβ line compared to an unconstrained fit, and consequently we abandoned this strategy.

In the following analysis we adopt a conservative approach, in order to avoid the risk of over-interpreting the fits: the line decomposition is not unique, and depends on the signal-to-noise ratio and the spectral resolution of the observations. Our principal aims are to ascertain the presence of an underlying broad component, measure its extent, and quantify the velocity scatter between the different gas clouds that we are able to identify along the line of sight.

In Fig. 12 we display the distribution of the [O III] $\lambda 5007$ velocity dispersion (corrected for thermal and instrumental effects) for all components found in NGC 5455 (red curve) and NGC 5471 (blue curve). The two curves are quite similar, increasing steeply with decreasing σ, below 25 km s^{-1}. The sharp drop seen at $\sigma < 8$ km s^{-1} is likely due to our inability to measure line widths approaching our spectral resolution. The histograms obtained from the single-Gaussian fits (in solid yellow and green) are much narrower. Values $\sigma > 25 - 30$ km s^{-1} measured from the multiple Gaussian profile fits refer to underlying broad components found throughout the extent of the H II regions, that cannot be uncovered by single Gaussian fits (see Sect. 5.1). The high intensity portion of each profile is composed of narrower, often multiple, components, with $\sigma < 20 - 25$ km s^{-1}. This dichotomy, that explains the presence of two different regimes in the multipple Gaussian histograms, is indicated in the plot.

Fig. 12 illustrates how a large fraction of the components resulting from our multiple Gaussian analysis ex-
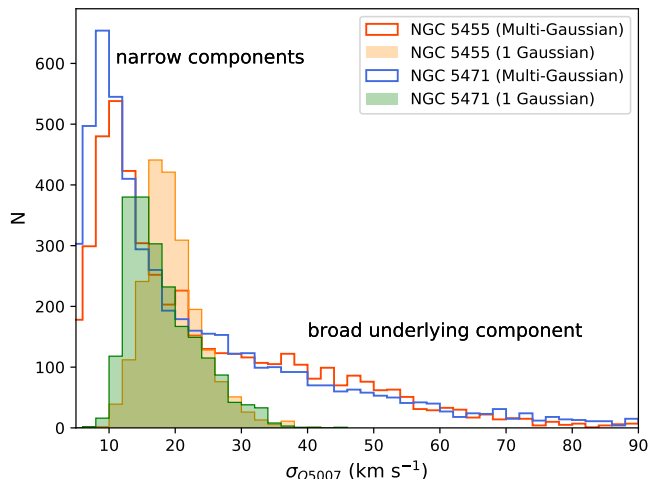
Figure 12. Histograms of the [O III] $\lambda 5007$ velocity dispersion from the multiple Gaussian analysis of NGC 5455 (red curve) and NGC 5471 (blue curve). The narrower histograms from the single Gaussian fits are also shown: NGC 5455 (solid yellow) and NGC 5471 (solid green).

hibits line widths near or below the sound speed (around 11 km s^{-1}), whereas single Gaussian fits are characterized by supersonic widths in virtually all cases. At higher spectral ($\sigma_{instr} = 3$ km s^{-1}) and spatial (0.1 pc) resolution Melnick et al. (1999) found that *all* the components they measured in 30 Dor have subsonic line widths, except for a pervasive, broad underlying one. They concluded that the combination of multiple discrete filaments, shells and gas clumps, each characterized by a narrow velocity dispersion, is responsible, in the case of 30 Dor, for the supersonic line profile width observed at lower spectral resolution, in agreement with the conclusion drawn by Chu & Kennicutt (1994). In our study we observe supersonic narrow subcomponents, but we cannot discard the possibility that they, too, would break up into narrower, subsonic profiles, if observed at higher spectral and, importantly, spatial resolution, since our seeing-limited line of sight integrates the kinematic information over $\sim$30 pc in the plane of the sky. In fact, the line profile of each spaxel results from a combination of individual filament profiles and the velocity distribution of all the filaments whose light contributes to the spaxel. Spatial resolution plays therefore a pivotal role in disentangling the kinematic superposition of discrete gas elements. This affects the number of separate components revealed by the multiple profile analysis, and implies that averaging over large apertures (e.g. for the derivation of global profiles – see Sect. 3) produces broad, supersonic profiles, even when the individual gas cloudlets are characterized by much narrower, subsonic line profiles. Ultimately, comparative conclusions on the widths of the line profiles of extragalactic H II regions need to take into account the vastly different physical resolutions attained by different studies: 1 arcsec corresponds to 33 pc at the distance of M101, 4 pc in M33 and only 0.25 pc in the LMC. In this context it is worth mentioning that the work on NGC 604 by Yang et al. (1996), carried out at higher spectral and physical spatial resolution than our present investigation, found supersonic line widths virtually everywhere in the nebula, based on *single* Gaussian

fits. As illustrated above, only the nearby 30 Dor nebula has been entirely resolved into subsonic components.

We show representative examples of our multiple profile fits for NGC 5471 in Fig. 13. We include clearly split or asymmetric line profiles (panels 1, 2, 5, 8), a spaxel in the SNR-hosting NGC 5471 B (panel 2), line models that include a broad and faint component (panels 3, 6, 7, 8), and a simple profile modeled with only two components (panel 4). The asymmetry seen in panels 5 and 8, where an extended wing is detected at red wavelengths (positive velocities), is typical of the SW region of NGC 5471, which appears to be dominated by shell structures, as discussed in Sec. 4.1. In general, we find complex line profiles, decomposed into multiple Gaussians, in regions where we have evidence for the presence of shells. This is similar to what is observed, at much higher spatial resolution, in the nearby 30 Dor (Torres-Flores et al. 2013).

5.1 Broad line components

Broad line components have been observed in spatially resolved observations of extragalactic H II regions and starburst galaxies (Yang et al. 1996; Melnick et al. 1999; Westmoquette et al. 2007; Bosch et al. 2019). These broad features (or wings) are likely due to stellar winds from massive stars and supernova explosions affecting the surrounding interstellar medium. Melnick et al. (1999) speculated that the ubiquitous broad component ($\sigma \sim 45$ km s^{-1}) they detected in the central parts of 30 Dor is the outcome of photo-erosion of dense gas clouds, producing a diffuse and highly turbulent gas component. In a similar vein, Westmoquette et al. (2007) proposed that the broad emission they measured for the starburst galaxy NGC 1569 ($\sigma \sim 40 - 120$ km s^{-1}) originates at the surface of cold clumps immersed in hot stellar winds. They invoked the presence of a turbulent mixing layer (Begelman & Fabian 1990), formed at the interface between the dense clouds and the stellar winds, which can give rise to emission lines featuring broad wings (Binette et al. 2009). The detection of broad underlying line profiles ($\sigma \sim 20 - 65$ km s^{-1}) at the edges of cold gas pillars in the vicinity of galactic ionizing clusters by Westmoquette et al. (2010, 2013) lends support to this interpretation.

A broad underlying component was detected for a large fraction ($\sim 2/3$) of the line profiles we examined in NGC 5455 and NGC 5471, typically having $\sigma = 30 - 50$ km s^{-1}, which is comparable to the widths found in 30 Dor (Melnick et al. 1999; Torres-Flores et al. 2013). In certain regions of NGC 5471, namely in the vicinity of knots A, B and C, we measured considerably larger widths, $\sigma > 80 - 100$ km s^{-1}. At these locations we detect very extended low-intensity profiles, examples of which can be seen in panels 2, 3 and 6 of Fig. 13.

5.1.1 Full width at zero intensity

At each spaxel we calculated the Full Width at Zero Intensity (FWZI), defined by the velocity range within which the line profile lies above the rms scatter of the continuum (such a definition is subjective and dependent on the signal-to-noise ratio, making quantitative comparisons between different investigations difficult). We compared the spatial distribution of the FWZI and the maximum σ of the line profiles, which is dominated by the presence of the underlying broad component. We found quite a good correlation, which indicates that even without performing a multi-profile fit one could use the FWZI as a proxy for the width of the broad component, thus simplifying the profile analysis, and offering a method to investigate the presence of underlying broad components even utilizing lower spectral resolution and independent of the accuracy of a multi-component analysis.

Fig. 14 illustrates the case of the Hβ line in NGC 5471. The FWZI can be somewhat affected by the presence of line splitting, which broadens the overall line profiles, but the effect is on the order of 50 km s^{-1}, while we typically measure FWZI values of several hundred km s^{-1}, up to > 1000 km s^{-1}. In our profile decompositions broad underlying components appear to have a minimum $\sigma \approx 25 - 30$ km s^{-1}. Fig. 14 shows that the presence of the broad component occurs throughout the area we examined, except approaching the south and west edges of the field of view. Adopting the interpretation introduced at the beginning of this Section, the map therefore suggests that the influence of massive star winds on the turbulent motion of the gas in a giant H II region is indeed ubiquitous, as found by Melnick et al. (1999, on a scale of 80 pc), extending roughly 250 pc from the centre of NGC 5471.

Maps of the FWZI for the Hβ and [O III] $\lambda 5007$ lines in both our targets are displayed in Fig. 15. Their appearance is very different compared to the σ maps presented in Fig. 9 - 10, obtained from single Gaussian fits. In regions located away from the main star-forming knots we measure FWZI $\simeq$ 300-500 km s^{-1}, while at the position of some of the main star-forming knots the FWZI can be much larger (> 700 km s^{-1}).

5.1.2 Evidence for supernova remnants

Observed at sufficiently high spectral resolution the line profiles of extragalactic SNRs appear broader than those of H II regions (Points et al. 2019). In most cases a narrow component (from unshocked H II region gas – $\sigma < 30$ km s^{-1}) sits on top of a broad component (shocked gas) with $\sigma \sim 40 - 100$ km s^{-1} (Blair et al. 1988; Dunne et al. 2000). In the case of NGC 5471 B, CK86 measured $\sigma(\text{broad}) \simeq 62$ km s^{-1} for Hα. Our map in Fig. 14 indicates a much larger value for Hβ, $\sigma(\text{broad}) \simeq 250$ km s^{-1}, because it refers to the much fainter extended component (visible – for [O III] $\lambda 5007$ – in panel 2 of Fig. 13). The analysis of the much brighter broad component is presented in Sect. 7.

In addition to NGC 5471 B, CK86 found large low-intensity velocity widths in the line profiles of NGC 5471 A and C, with FWZI(Hα) = 445 km s^{-1} and 300 km s^{-1}, respectively. With deeper echelle spectra, Chen et al. (2002) measured FWZI(Hα) $\simeq 620$ km s^{-1} for NGC 5471 B. Our measurements are in the range FWZI(Hβ) $\simeq 400 - 1300$ km s^{-1} and FWZI([O III] $\lambda 5007$) $\simeq 750 - 1300$ km s^{-1}. The largest values are found in NGC 5471 C (Hβ) and NW of the centre of NGC 5471 A ([O III] $\lambda 5007$).

It is worth pointing out that the linear diameters of SNRs in M101 measured by Franchetti et al. (2012) from *HST* images, and classified as due to core-collapse SNe, is in the range $20 - 80$ pc: at our seeing-limited resolution of about 30 pc we can expect to barely resolve a typical SNR
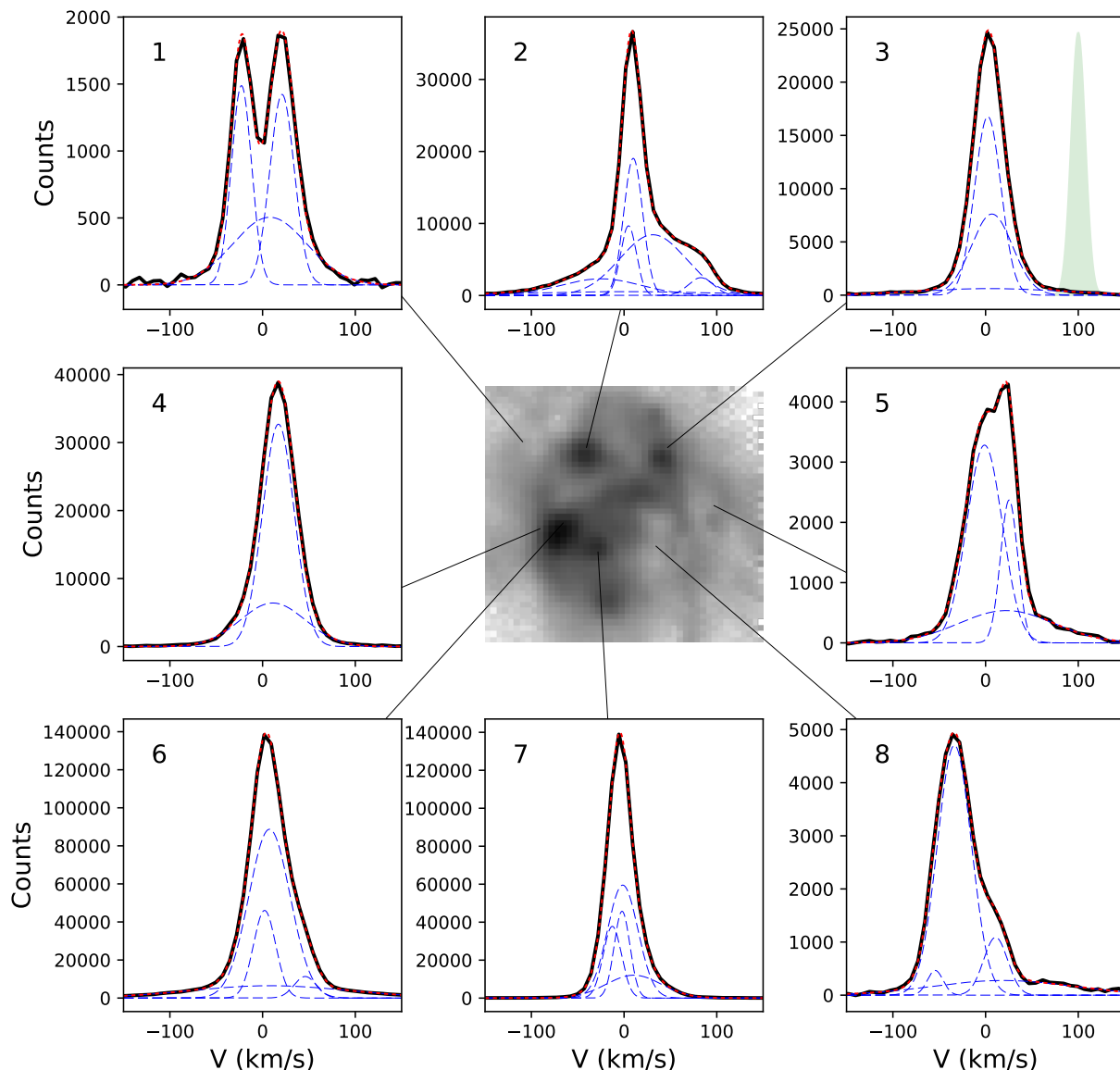
Figure 13. Representative examples of multiple profile fits to the [O III] λ5007 line for NGC 5471. In each panel we display the observed line profile as a black continuous line, the model fit as a dotted red line, and the different model components as dashed curves. The green filled Gaussian at the right in panel 3 represents the instrumental profile.

in this galaxy. High spatial resolution images by Chen et al. (2002) show that the SNR in NGC 5471 B, identified as a resolved [S II]-bright shell, is approximately 2 arcsec in diameter, which is twice our seeing.

Based on the finding by Sramek & Weedman (1986) that both NGC 5471 A and B have nonthermal radio emission, a signature of the presence of a SNR, CK86 suggested that all the three main knots in NGC 5471 (A, B and C) could host SNRs. The fact that these regions stand out so clearly in the maps of Fig. 14−15 supports their suggestion. FWZI([O III] λ5007) in NGC 5455 A peaks at 750 km s^{-1}, suggesting a similar interpretation, although we are unaware of the discovery of SNR signatures (nonthermal radio emission or indications of shocked gas from optical emission line ratios) in this object. SN 1970G (whose location is shown in Fig. 1) exploded to the NW of NGC 5455 A.

In NGC 5471 C Castañeda et al. (1990) measured a very

large FWZI(Hα) ≃ 3300 km s^{-1}. We do not confirm such an extreme value, possibly due to the lower signal-to-noise ratio of our Hβ line. Integrating the flux in a 2 × 2 arcsec^2 region centred on this knot, in order to increase the signal-to-noise ratio, we obtain FWZI(Hβ) ≃ 2100 km s^{-1}, which is considerably larger than for any other knot (⩽ 750 km s^{-1}). We find FWZI([O III] λ5007) ≃ 1450 km s^{-1}. We thus confirm the presence of a remarkable low-intensity velocity extension of the Balmer lines in NGC 5471 C.

We find it interesting that NGC 5471 A, B and C, around which we detect large FWZIs, are three of the four most Hα-luminous clusters in this complex (García-Benito et al. 2011). However, the most Hα-luminous cluster after knot A is knot A′, which does not exhibit a particularly large FWZI or σ(broad). This suggests that the effect of something besides the energy output of 'living' massive stars,

FWZI

km/s

σ (max)
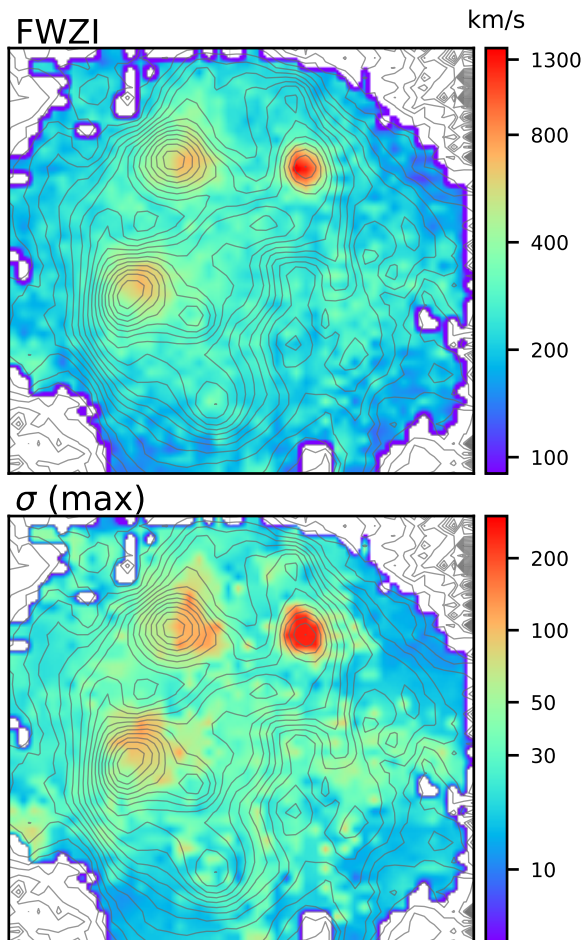
Figure 14. Spatial distribution of the FWZI (top) and maximum velocity dispersion (bottom) of the Hβ line for NGC 5471.

namely supernova explosions, is required to generate a broad low-intensity profile.

5.1.3 Velocity structures and evidence for shells

In the left panels of Fig. 16 we look at the velocity difference between the single Gaussian centroid (representative of the bright, narrow part of the line profile) and the broad component centroid (the midpoint of the FWZI range) for the [O III] λ5007 line. Significant deviations ($+60$ km s^{-1}) between these quantities are localized in the 'shell areas' NW of the centre in NGC 5455 and SW of the centre in NGC 5471, suggesting that at these locations the weak, broad profile component is decoupled from the stronger narrow components. In the rest of the field of view the difference is generally small and on average zero. These two areas match the locations of largest splitting of the composite line profiles, measured by the rms dispersion of the central velocities of the narrow components, shown in the map of the right panels of Fig. 16. This figure provides similar information as, and is generally consistent with, the single Gaussian σ maps shown in Fig. 9 and 10.

Since line splitting is expected in the presence of expanding gas shells or multiple moving filaments, the maps of the velocity scatter are consistent with the idea that the two

areas defined earlier are populated by expanding shells and filaments moving at different velocities along the line of sight (see also our discussion of Figures 9–10), for which we measure an rms dispersion of the central velocities of the multiple narrow components of up to $\sim$100 km s^{-1}. Line splitting at the $20-40$ km s^{-1} level is widespread in our fields, a manifestation of the complex internal kinematics of these two giant H II regions, as already demonstrated by the line profiles shown in Fig. 7–8.

6   GLOBAL SUPERSONIC LINE WIDTHS

We can now return briefly to the supersonic line widths exhibited by the global profiles presented in Sect. 3.1, and which is typical of giant H II regions. For the best-studied case, 30 Dor, Chu & Kennicutt (1994) and Melnick et al. (1999) demonstrated that the integrated profile breaks up into discrete components of subsonic widths. Melnick et al. (2019) have shown that the supersonic width of 30 Dor is in fact due to macroscopic gas elements moving inside the gravitational potential of the region. In addition, the presence of stellar winds plays a considerable role in the overall dynamics.

Melnick et al. (2019) tested this conclusion, by showing that the integrated line width is comparable to the rms dispersion of the radial velocity measured across the face of the nebula. This procedure cannot be used in our case: the velocity dispersion is 'diluted' by the $\sim$140$\times$ coarser physical spatial resolution, down to $5-8$ km s^{-1}. We have instead performed a consistency test, by calculating the intensity-weighted rms dispersion obtained from the velocity decomposition of the line profiles (the single-spaxel results are shown in Fig. 16). Although we cannot expect perfect agreement with the width of the integrated line profiles, due to the unavoidable difficulties intrinsic to multiple Gaussian fits, we should find a similar value. We limit the comparison to the [O III] λ5007 lines, because of the higher signal-to-noise ratio, but above all because of the much smaller smearing from thermal broadening. For NGC 5455 we find a weighted rms dispersion of 15.7 km s^{-1}, and for NGC 5471 a value of 22.2 km s^{-1}. These results compare favorably with the integrated line widths (see Table 1), particularly in the case of NGC 5471.

We conclude that our data provide evidence that the major contributor to the supersonic turbulence measured in giant H II regions (excluding the underlying components) is the motion of discrete macroscopic cloudlets, in agreement with Melnick et al. (2019).

The stellar masses of our target H II regions can be obtained from their narrow-band luminosities from

$$\log(M^*/M_\odot) = \log[L(H\beta)] - 33.15. \qquad (3)$$

This equation was obtained from instantaneous burst models calculated with Starburst99 (Leitherer et al. 1999), integrating a Salpeter initial mass function over the range $0.2 - 100\, M_\odot$. From the Hβ luminosities published by Fernández Arenas et al. (2018) we derive very similar masses for NGC 5455 and NGC 5471, $\log(M^*/M_\odot) \sim 6.7 - 6.8$.

It is instructive to compare these photometric masses
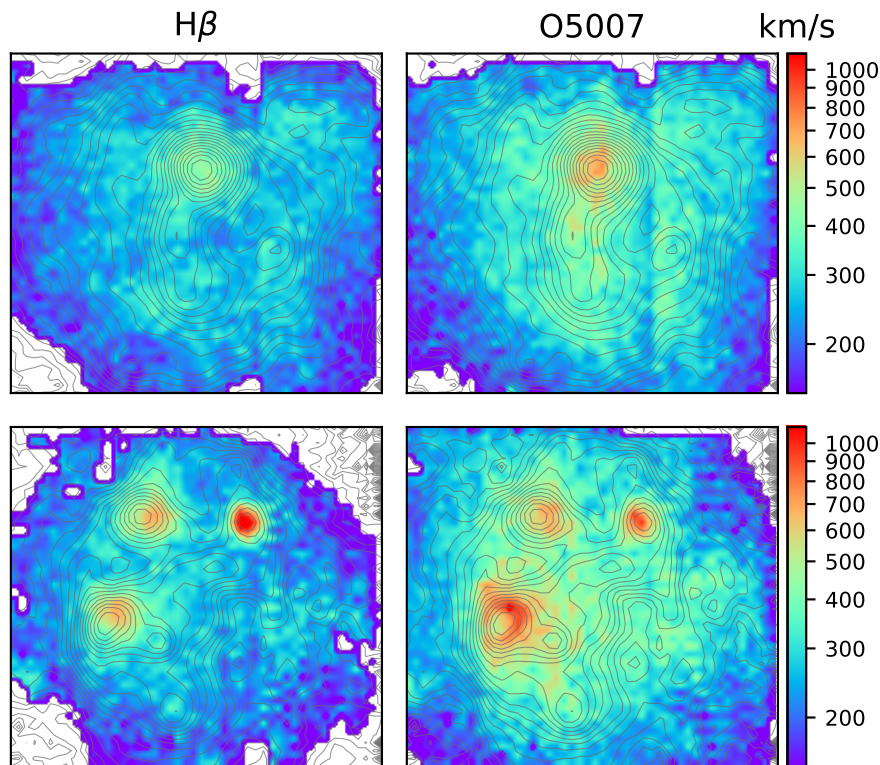
Figure 15. FWZI maps of the Hβ and [O III] λ5007 lines for NGC 5455 (top) and NGC 5471 (bottom). The same velocity range is used in order to facilitate the comparison between the two H II regions.

with estimates of the dynamical masses, assuming that their global gas motions are due to gravity. From the virial theorem the velocity dispersion is related to the mass as follows:

$$\sigma = \left(\frac{GM_d}{\eta R_{eff}} \right)^{0.5} \tag{4}$$

where R_{eff} is the effective radius enclosing half of the mass, and η is on the order unity. Taking a stellar mass of $6 \times 10^6 \, M_\odot$, derived from the ionizing flux, we obtain $\sigma \simeq 21 \, \mathrm{km \, s^{-1}}$, close to the observed global values (see Table 1), if we assume $R_{eff} = 60 \, \mathrm{pc}$. Although we cannot measure R_{eff} directly, this value appears plausible.

7   THE SUPERNOVA REMNANT IN NGC 5471 B

NGC 5471 B hosts a SNR, as first shown by Skillman (1985). We detect a bright and broad line component associated with it across a region of $\sim$90 pc in diameter.

The Hβ and [O III] λ5007 line profiles, integrated over a $2 \times 2 \, \mathrm{arcsec^2}$ region centred on the Hβ peak, are displayed in Fig. 17. We have decomposed each profile using a two-component Gaussian fit, which works reasonably well in this restricted area, in order to focus on the two main features: the narrow central component, attributed to the host H II region (dashed line) and the high-intensity broad component, attributed to the SNR (dotted line) (we are therefore not fitting the even broader low-intensity wings that were analysed in Sect. 5.1). In the case of Hβ we find a narrow component line width, corrected for thermal, instrumental and fine

structure effects, of $\sigma_n^0(\mathrm{H}\beta) = 9.6 \pm 0.1 \, \mathrm{km \, s^{-1}}$, while for the broader component we measure $\sigma_b^0(\mathrm{H}\beta) = 59.2 \pm 0.4 \, \mathrm{km \, s^{-1}}$. CK86 reported an uncorrected value $\sigma_b(\mathrm{H}\alpha) = 61.6 \, \mathrm{km \, s^{-1}}$, virtually equal to our $\sigma_b(\mathrm{H}\beta) = 60.7 \pm 0.4 \, \mathrm{km \, s^{-1}}$. Chen et al. (2002) measured $\sigma_n(\mathrm{H}\alpha) = 17.4 \pm 0.8 \, \mathrm{km \, s^{-1}}$ (compared to our $16.4 \pm 0.1 \, \mathrm{km \, s^{-1}}$) and $\sigma_b(\mathrm{H}\alpha) = 62.8 \pm 2.1 \, \mathrm{km \, s^{-1}}$. There is therefore full consistency between these independent measurements.

We notice several differences between the Hβ and [O III] profile decompositions. For [O III] λ5007 both components are narrower than in the case of Hβ: $\sigma_n^0([\mathrm{O \, III}]) = 8.6 \pm 0.1 \, \mathrm{km \, s^{-1}}$ and $\sigma_b^0([\mathrm{O \, III}]) = 41.8 \pm 0.3 \, \mathrm{km \, s^{-1}}$. The flux of the broad component relative to that of the narrow component is also smaller: $f_b/f_n([\mathrm{O \, III}]) = 1.03$ vs. $f_b/f_n(\mathrm{H}\beta) = 1.67$. Moreover, while for H$\beta$ the broad component is well aligned with the velocity of the narrow component, for [O III] the broad component is shifted to higher velocities (by $\sim$12 $\mathrm{km \, s^{-1}}$). We point out that for both lines the integrated narrow component has a slightly subsonic line width.

In the case of NGC 5471 B a single Gaussian fails miserably to fit the line profile, due to the presence of the intense broad component. In order to describe the overall line width we adopt the FWHM measured from the model profile (indicated in Fig. 17) and define a 'pseudo standard deviation', $\sigma^* \equiv \mathrm{FWHM}/2.355$. For lines that are approximately following a Gaussian profile, $\sigma \simeq \sigma^*$, but in the presence of significant deviations from the Gaussian line shape σ^* is a better representation of the line width. We can see from the numerical results reported in Fig. 17 that at half peak intensity the Hβ line is 5.2 $\mathrm{km \, s^{-1}}$ wider than [O III], which

Δ centroid   velocity scatter
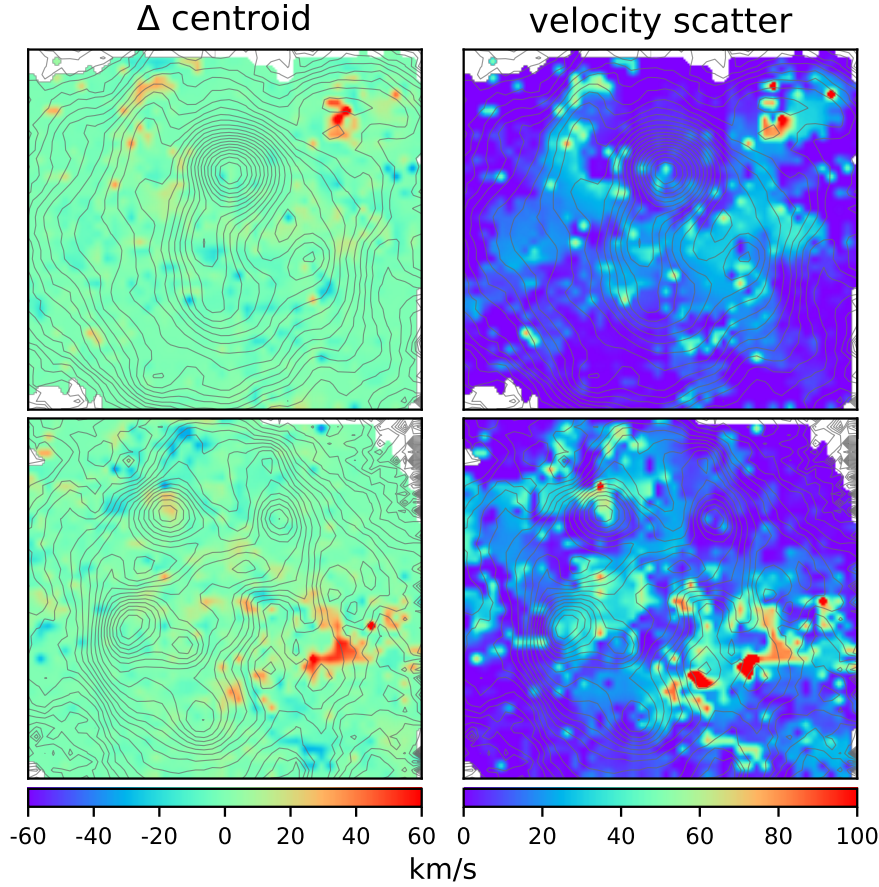
Figure 16. (Left) Maps of the velocity difference between the single Gaussian centroid and the broad component centroid. (Right) Maps of the velocity scatter between the narrow components revealed by the multiple Gaussian fits, measured by the rms dispersion of their central velocities. NGC 5455 is at the top and NGC 5471 is at the bottom. All maps refer to the [O III] $\lambda5007$ line.

results from the combined contribution of the larger values of both σ_n and σ_b.

Deeper insight into the kinematics and excitation properties of NGC 5471 B can be gained from the maps shown in Fig. 18. These refer to a $3.5 \times 3.5\,\mathrm{arcsec}^2$ section of the full-resolution data cube, centred on the Hβ emission peak. The panels in this figure display maps of different quantities measured from a two-component fit to Hβ (top row) and [O III] $\lambda5007$ (bottom row). The first column of Fig. 18 shows how the velocity offset between narrow and broad components is negligible for Hβ, but peaks around $20\ \mathrm{km\,s^{-1}}$ for [O III] – a behaviour already established from the integrated line profiles of Fig. 17. The width of the broad components peaks to the west of the Hβ emission peak (second column), but is significantly larger for Hβ. Differences such as these are understood as a consequence of the fact that the two emission lines are formed at different temperatures in the recombination flow associated with a radiative supernova shock (Lasker 1977), and therefore they refer to different gas filaments. In the third column we show maps of the width of the narrow component σ_n. They are completely different from the σ_b maps, showing similarity between Hβ and [O III], as well as subsonic line widths in the central, brightest parts of NGC 5471 B.

In the top panel of the final column we show a map of the flux ratio between the broad and the narrow Hβ compo-

nents. The ratio peaks in the NW sector. The bottom panel of the same column shows that in the same NW sector the gas excitation of the broad component, measured by the [O III]/Hβ line ratio, reaches its minimum value. In Sect. 3 we explained such a low [O III]/Hβ ratio with the presence of an interstellar shock at low metallicity. With the help of the *HST*-based study by Chen et al. (2002) we identify the low-excitation sector with the shell revealed by their [S II]/Hα line ratio map. The western edge of this $\sim$2 arcsec-wide shell, where the [S II]/Hα is higher, corresponds approximately to the position where we measure the largest σ_b. The top right panel of Fig. 18 then shows that the strength of the broad component relative to the narrow component peaks near the centre of the shell.

8   Hβ vs. [O III] LINE WIDTHS

Hippelein (1986) noted that the integrated line widths of extragalactic giant H II regions, corrected for thermal broadening, differ systematically between H I and [O III] lines, finding $\sigma(H\alpha) - \sigma([\mathrm{O\ III}]\,\lambda5007) \simeq 2\ \mathrm{km\,s^{-1}}$. A comparable result was obtained for H II galaxies by Bordalo & Telles (2011). Our integrated measurements for NGC 5455 and NGC 5471, presented in Table 1, are in agreement with these findings. Moreover, in a fashion similar to our profile decomposition for NGC 5471 B, presented in Sect. 7 and shown in Fig. 17,
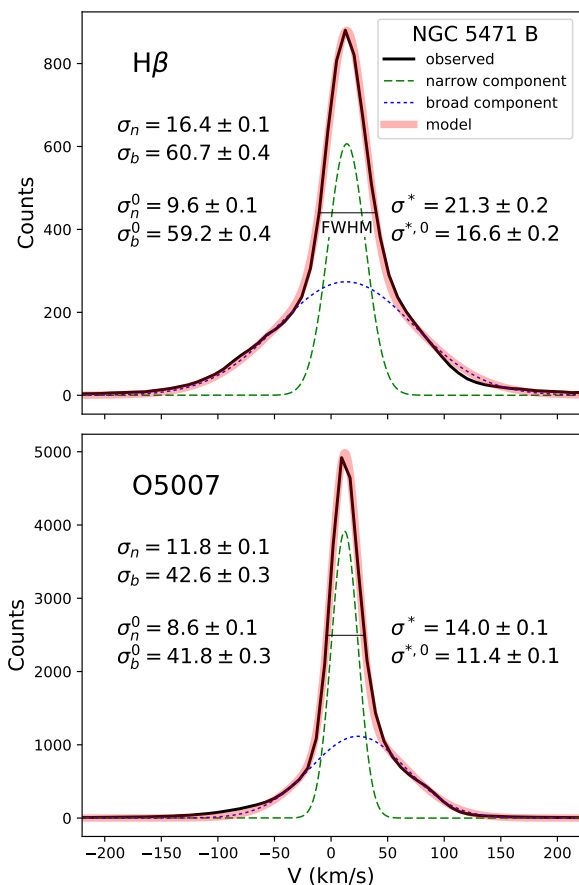
Figure 17. Integrated Hβ (top) and [O III] $\lambda5007$ (bottom) line profiles of NGC 5471 B (black profile). The decomposition into a narrow (green dashed line) and a broad (blue dotted line) Gaussian components results in the model shown in red. The measured widths σ are reported, in km s^{-1}, for both the narrow (n) and the broad (b) components. Widths corrected for thermal and instrumental effects (plus fine structure for Hβ) are indicated as σ^0. A 'pseudo standard deviation' σ^* is measured from the FWHM of the model (indicated), with $\sigma^{*,0}$ its corrected value.

we carried out a two-Gaussian fit to the integrated Hβ and [O III] $\lambda5007$ line profiles of both NGC 5455 and NGC 5471. The results are presented in Fig. 19. It can be seen that the line width difference between Hβ and [O III] $\lambda5007$ is confirmed for both the (corrected) narrow components (σ_n^0) and the composite model width ($\sigma^{*,0}$), albeit with somewhat differing magnitudes.

We inspected the line width discrepancy between Hβ and [O III] in the brightest star-forming knots of our two targets (NGC 5471 A, A$'$, B, C, E and NGC 5455 A), defining 2×2 arcsec^2 regions centred at their positions. We decomposed their line profiles, following the method outlined in Sect. 5, and calculated the FWHM of the model profile. As explained in Sect. 7 we define $\sigma^* \equiv$ FWHM/2.355, obtaining a mean, corrected value difference $\sigma^{*,0}(H\beta) - \sigma^{*,0}([O III] \lambda5007) = 1.7 \pm 0.8$ km s^{-1} (we excluded NGC 5471 B, for which the difference is considerably larger than the rest: 5.2 km s^{-1} – see Sect. 7). The result is virtually unchanged using single Gaussian fits: $\sigma(H\beta) - \sigma([O III] \lambda5007) = 1.5 \pm 0.7$ km s^{-1}, with the distinction that the profile decomposition reveals the separate

contribution of narrow and broad components to the overall profile. In conclusion, the tests we carried out confirm a line width offset of about $1-2$ km s^{-1} between the Hβ and [O III] line profiles, both globally and for individual star forming cores.

We examined how the Hβ and [O III] line width difference varies with position in NGC 5455 and NGC 5471, by taking the results of our multiple Gaussian fits (Sect. 5), and considering the σ^* widths of the model profiles. The grey dots in the left panels of Fig. 20 represent the difference $\Delta\sigma^* = \sigma^*(H\beta) - \sigma^*([O III] \lambda5007)$ measured in each spaxel. The increasing spread with decreasing line flux is largely due to random uncertainties in our measurements. In order to assess the magnitude of these uncertainties, we represent with red dots the σ^* difference obtained using the [O III] lines at $\lambda4959$ and $\lambda5007$. These two lines should yield the same width, so that measurement uncertainties are now (approximately) represented in the plot. The comparison between grey and red dots indicates that only positive $\Delta\sigma^*$ values for the brightest spaxels should be deemed as significant. We conservatively isolated these spaxels to be those contained in the area of the plot above the dotted line. Their spatial location and $\Delta\sigma^*$ values are shown in the central panels of Fig. 20. Most points correspond to $\Delta\sigma^* \simeq 2 - 3$ km s^{-1}, with the notable exception of NGC 5471 B, where the width difference increases to 13 km s^{-1} – as shown in Sect. 7 this is related to the strong contribution from the SNR to the line profile. The right panels display the gas excitation map, using the [O III] $\lambda5007$/Hβ line ratio. We fail to discern obvious correlations between $\Delta\sigma^*$ and gas excitation (except again for the case of NGC 5471 B, where the excitation reaches a minimum – see Sect. 7), as well as differences between star-forming cores and diffuse gas. Admittedly, the fractional coverage of the spaxels that survived our selection in the central panel of Fig. 20 is small, but to our knowledge this is the first time that the width discrepancy between hydrogen and metal lines is examined on a spatially-resolved basis.

The explanation for the systematic line width difference between recombination and collisionally excited lines of photoionized nebulae continues to elude us. However, we find it remarkable that the line width difference is quantitatively comparable (~2 km s^{-1}) among giant H II regions and the more luminous ensembles of giant ionized nebulae in H II galaxies, and between giant H II regions and objects like the Orion nebula (O'Dell et al. 2003) that are more than three orders of magnitude less luminous. These similarities suggest a common origin. The disparity of kinematical conditions between small and giant H II regions is such that smearing of fine details of non-Gaussian line profiles by thermal broadening (García-Díaz et al. 2008) appears as a less likely explanation than an interpretation based on physical attributes of the nebular gas (O'Dell et al. 2017). This conclusion is supported by the fact that, at least in the Orion nebula, H I and He I recombination lines have virtually the same width (O'Dell et al. 2017), while a significant reduction of line smearing due to thermal broadening (approximately a factor of two according to Eq. 2) should be observed for He I lines instead. Work is under way to address these issues in a future publication concerning a sample of giant extragalactic H II regions.
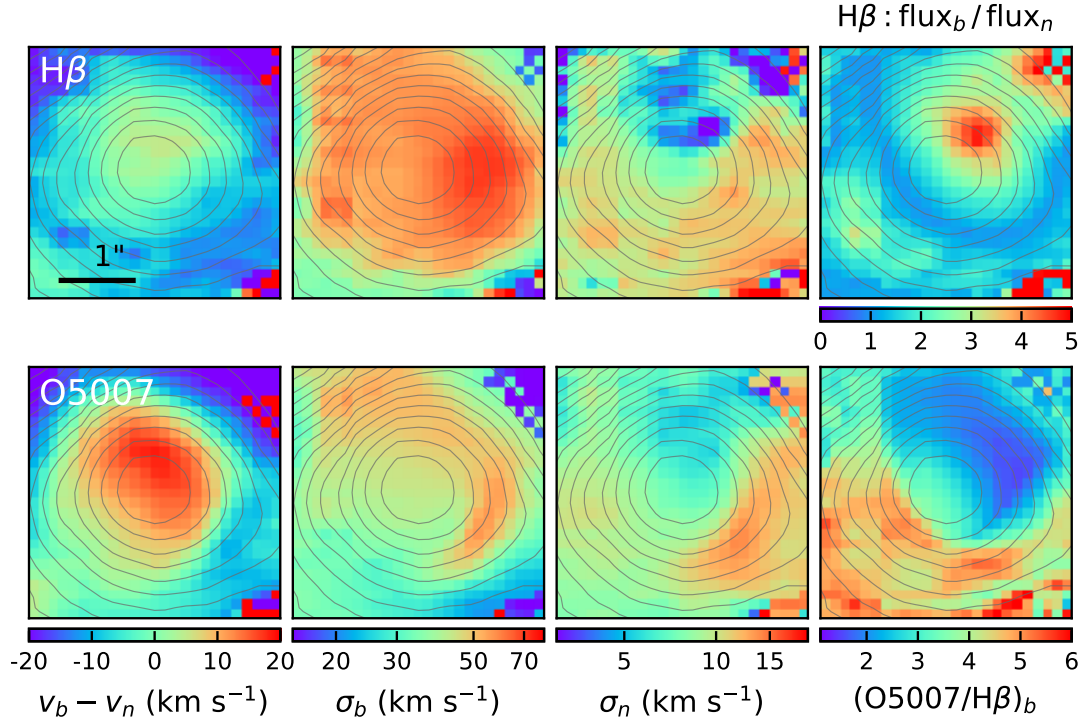
Figure 18. Kinematic and excitation maps of NGC 5471 B derived from two-component fits to the Hβ (top row) and [O III] λ5007 (bottom rows) lines. The quantities shown in the first three columns are the velocity offset between the broad and narrow components ($v_b - v_n$), and the line widths of the broad (σ_b) and narrow (σ_n) components. In the last column we show the relative Hβ flux between the two components (top) and the [O III]/Hβ line ratio for the broad component (bottom).
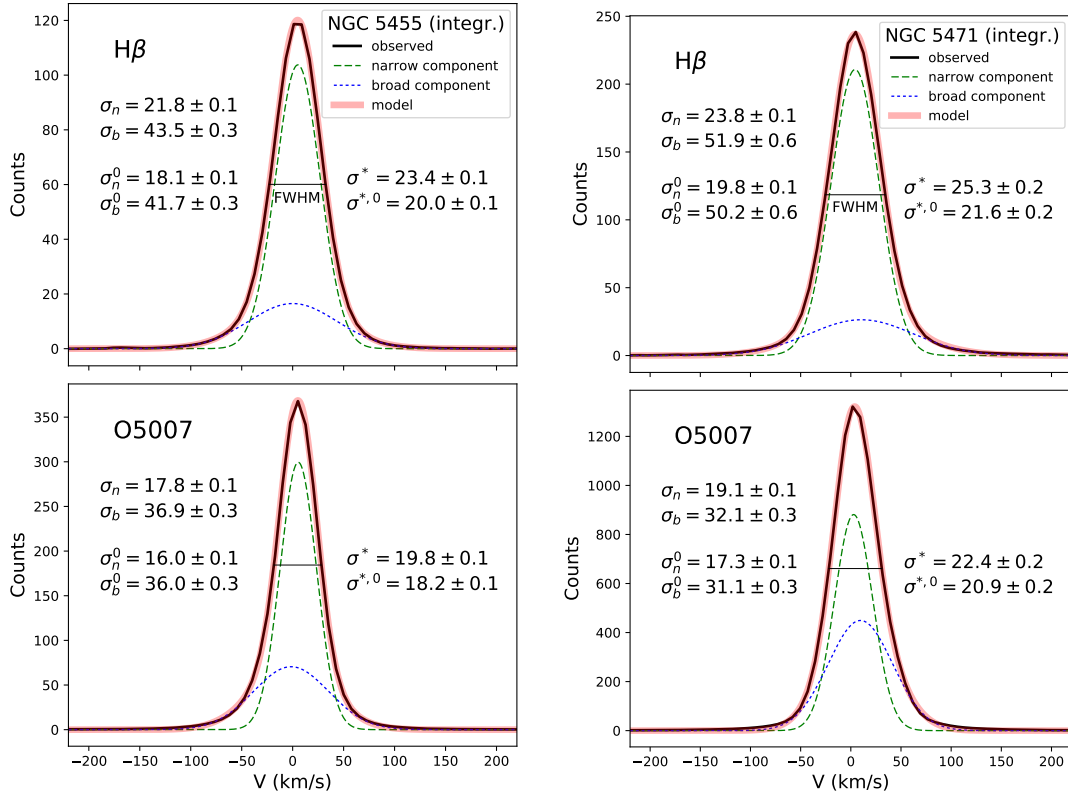
Figure 19. Two-Gaussian decomposition of the integrated Hβ and [O III] λ5007 line profiles for NGC 5455 (left) and NGC 5471 (right). See Fig. 17 for an explanation of the different line types and quantities reported.
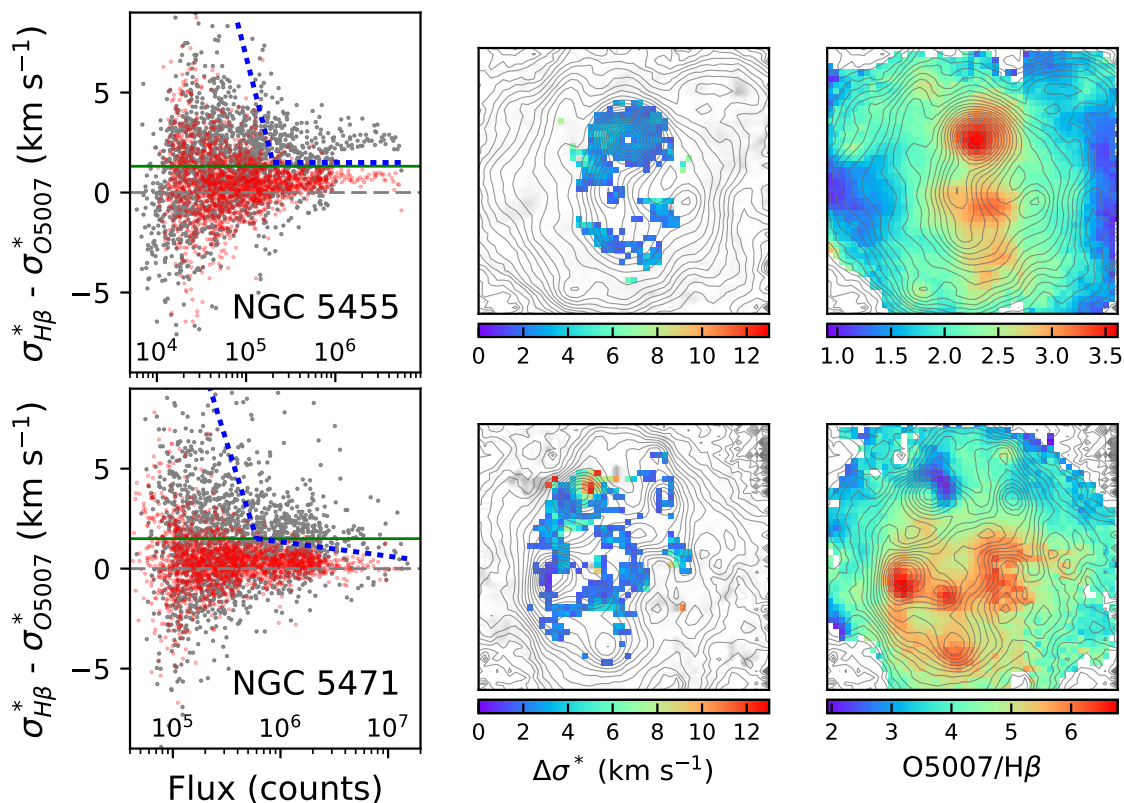
Figure 20. (Left) Line width difference $\Delta\sigma^* = \sigma^*(H\beta) - \sigma^*([\text{O\,III}]\,\lambda 5007)$ as a function of the [O\,III] $\lambda 5007$ flux measured from multiple Gaussian line fits (grey dots). Red dots represent the width difference measured between [O\,III] $\lambda 4959$ and $\lambda 5007$ lines, in order to estimate the $\Delta\sigma^*$ uncertainties. The horizontal dashed line is drawn at $\Delta\sigma = 0$, while the mean $\Delta\sigma^*$ difference is shown by the continuous green line. The blue dotted lines isolate the spaxels for which $\Delta\sigma^*$ is considered to be significant. NGC 5455 is at the top, NGC 5471 at the bottom. (Center) Maps of $\Delta\sigma^*$ for the spaxels isolated in the left panels. (Right) Maps of the [O\,III] $\lambda 5007/H\beta$ line flux ratio.

9   SUMMARY

We have studied the kinematics of the giant H II regions NGC 5455 and NGC 5471, located in the galaxy M101, using integral field data obtained with the Keck Cosmic Web Imager. We have fitted the profiles of the Hβ and [O\,III] $\lambda 5007$ lines using both single Gaussian curves and multiple Gaussian models. While the former technique cannot capture all the detailed information that the multiple profile approach can provide, the interpretation of the two types of fits has points in common that offer consistent results, but some important divergences emerge. Our main findings are listed below:

(i) both the $I - \sigma$ diagram (from single Gaussian fits) and the multiple profile analysis provide kinematic evidence for the presence of several expanding shells and moving filaments.

(ii) decomposing the line profiles using multiple Gaussians yields a large fraction of components with subsonic line widths. The single Gaussian fits instead provide only supersonic line widths – this outcome underlines the inadequacy of fitting single Gaussian curves to the line profiles of giant H II regions. We cannot exclude that at higher spectral and spatial resolution multiple Gaussian fits would split all 'narrow' supersonic components into subsonic ones.

(iii) an underlying broad component characterized by velocity widths $\sigma \simeq 30 - 50 \; \text{km\,s}^{-1}$ – possibly resulting from stellar wind interactions with cold gas – is commonly found in the bright parts of our two targets, extending across hundreds of pc. This component can be described by the full width at zero intensity of the line profiles, a quantity that is independent of the accuracy of the multiple line fitting.

(iv) the supersonic turbulence inferred from the global profiles is consistent with the combined contribution of individual gas cloudlets, and the dispersion of their velocities.

(v) for three bright star-forming knots in NGC 5471 (A, B and C) the large velocity spread $(750-1300 \; \text{km\,s}^{-1}$ in the case of [O\,III]) of the low-intensity component supports previous suggestions that all these regions host supernova remnants.

(vi) known and suspected supernova remnants in NGC 5471 stand out thanks to their low [O\,III]/Hβ line ratios relative to the surrounding gas – we attribute this to the low metallicity of the region.

(vii) the known supernova remnant in NGC 5471 B, barely spatially resolved in our data, displays remarkable differences between H\,I and [O\,III] emission lines.

(viii) we confirm the presence of a global, as well as a localized, systematic offset between the widths of the Hβ recombination line and the [O\,III] $\lambda 5007$ collisionally excited line,

which is independent of the gas excitation. We argue that its origin lies in the physics of the line-emitting gas rather than the larger thermal broadening of the Balmer lines.

ACKNOWLEDGMENTS

REFERENCES

Akaike H., 1974, IEEE Transactions on Automatic Control, 19, 716
Allen M. G., Groves B. A., Dopita M. A., Sutherland R. S., Kewley L. J., 2008, ApJS, 178, 20
Astropy Collaboration et al., 2013, A&A, 558, A33
Astropy Collaboration et al., 2018, AJ, 156, 123
Begelman M. C., Fabian A. C., 1990, MNRAS, 244, 26P
Binette L., Drissen L., Ubeda L., Raga A. C., Robert C., Krongold Y., 2009, A&A, 500, 817
Blair W. P., Chu Y. H., Kennicutt R. C., 1988, in Roger R. S., Landecker T. L., eds, IAU Colloq. 101: Supernova Remnants and the Interstellar Medium. p. 193
Bordalo V., Telles E., 2011, ApJ, 735, 52
Bordalo V., Plana H., Telles E., 2009, ApJ, 696, 1668
Bosch G., et al., 2019, MNRAS, 489, 1787
Bresolin F., Kennicutt R. C., Ryan-Weber E., 2012, ApJ, 750, 122
Castañeda H. O., 1988, ApJS, 67, 93
Castañeda H. O., Vilchez J. M., Copetti M. V. F., 1990, ApJ, 365, 164
Chávez R., Terlevich R., Terlevich E., Bresolin F., Melnick J., Plionis M., Basilakos S., 2014, MNRAS, 442, 3565
Chen C.-H. R., Chu Y.-H., Gruendl R., Lai S.-P., Wang Q. D., 2002, AJ, 123, 2462
Chen C.-H. R., Chu Y.-H., Johnson K. E., 2005, ApJ, 619, 779
Chu Y.-H., Kennicutt Jr. R. C., 1986, ApJ, 311, 85
Chu Y.-H., Kennicutt Jr. R. C., 1994, ApJ, 425, 720
Dittmann J. A., Soderberg A. M., Chomiuk L., Margutti R., Goss W. M., Milisavljevic D., Chevalier R. A., 2014, ApJ, 788, 38
Dunne B. C., Gruendl R. A., Chu Y.-H., 2000, AJ, 119, 1172
Fernández Arenas D., et al., 2018, MNRAS, 474, 1250
Firpo V., Bosch G., Hägele G. F., Díaz Á. I., Morrell N., 2011, MNRAS, 414, 3288
Franchetti N. A., et al., 2012, AJ, 143, 85
Gallagher J. S., Hunter D. A., 1983, ApJ, 274, 141
García-Benito R., Pérez E., Díaz Á. I., Maíz Apellániz J., Cerviño M., 2011, AJ, 141, 126
García-Díaz M. T., Henney W. J., López J. A., Doi T., 2008, Rev. Mex. Astron. Astrofis., 44, 181
González-Morán A. L., et al., 2019, MNRAS, 487, 4669
Hägele G. F., Díaz Á. I., Terlevich R., Terlevich E., Bosch G. L., Cardaci M. V., 2013, MNRAS, 432, 810
Hippelein H. H., 1986, A&A, 160, 374
Kass R. E., Raftery A. E., 1995, Journal of the American Statistical Association, 90, 773
Kennicutt R. C. J., 1984, The Astrophysical Journal, 287, 116
Kennicutt R. C., Bresolin F., Garnett D. R., 2003, ApJ, 591, 801
Lasker B. M., 1977, PASP, 89, 474
Leitherer C., et al., 1999, ApJS, 123, 3
Liddle A. R., 2004, MNRAS, 351, L49
Liddle A. R., 2007, MNRAS, 377, L74
Mac Low M.-M., McCray R., 1988, ApJ, 324, 776
Martínez-Delgado I., Tenorio-Tagle G., Muñoz-Tuñón C., Moiseev A. V., Cairós L. M., 2007, AJ, 133, 2892
Mathewson D. S., Clarke J. N., 1973, ApJ, 180, 725
Melnick J., 1977, ApJ, 213, 15
Melnick J., Moles M., Terlevich R., Garcia-Pelayo J.-M., 1987, MNRAS, 226, 849
Melnick J., Tenorio-Tagle G., Terlevich R., 1999, MNRAS, 302, 677
Melnick J., Terlevich R., Tenorio-Tagle G., Telles E., Terlevich E., 2019, arXiv e-prints, p. arXiv:1912.03543
Méndez D. I., Esteban C., 1997, ApJ, 488, 652
Moiseev A. V., Lozinskaya T. A., 2012, MNRAS, 423, 1831
Morrissey P., et al., 2018, ApJ, 864, 93
Muñoz-Tuñón C., Gavryusev V., Castañeda H. O., 1995, AJ, 110, 1630
Muñoz-Tuñón C., Tenorio-Tagle G., Castañeda H. O., Terlevich R., 1996, AJ, 112, 1636
Newville M., et al., 2019, lmfit/lmfit-py 0.9.13, doi:10.5281/zenodo.2620617, https://doi.org/10.5281/zenodo.2620617
O'Dell C. R., Peimbert M., Peimbert A., 2003, AJ, 125, 2590
O'Dell C. R., Ferland G. J., Peimbert M., 2017, MNRAS, 464, 4835
Ott T., 2012, QFitsView: FITS file viewer (ascl:1210.019)
Points S. D., Long K. S., Winkler P. F., Blair W. P., 2019, arXiv e-prints, p. arXiv:1910.07007
Roy J.-R., Aube M., McCall M. L., Dufour R. J., 1992, ApJ, 386, 498
Sabalisck N. S. P., Tenorio-Tagle G., Castaneda H. O., Munoz-Tunon C., 1995, ApJ, 444, 200
Schwarz G., 1978, Annals of Statistics, 6, 461
Shi K., Huang Y. F., Lu T., 2012, MNRAS, 426, 2452
Shull P. J., 1983, ApJ, 275, 592
Skillman E. D., 1985, ApJ, 290, 449
Skillman E. D., Balick B., 1984, ApJ, 280, 580
Smith M. G., Weedman D. W., 1970, ApJ, 161, 33
Spitzer L., 1968, Diffuse matter in space. New York: Interscience Publishers
Sramek R. A., Weedman D. W., 1986, ApJ, 302, 640
Tenorio-Tagle G., Bodenheimer P., 1988, ARA&A, 26, 145
Tenorio-Tagle G., Munoz-Tunon C., Cox D. P., 1993, ApJ, 418, 767
Terlevich R., Melnick J., 1981, MNRAS, 195, 839
Torres-Flores S., Barbá R., Maíz Apellániz J., Rubio M., Bosch G., Hénault-Brunet V., Evans C. J., 2013, A&A, 555, A60
Westmoquette M. S., Exter K. M., Smith L. J., Gallagher J. S., 2007, MNRAS, 381, 894
Westmoquette M. S., Slavin J. D., Smith L. J., Gallagher J. S. I., 2010, MNRAS, 402, 152
Westmoquette M. S., Dale J. E., Ercolano B., Smith L. J., 2013, MNRAS, 435, 30
Yang H., Chu Y.-H., Skillman E. D., Terlevich R., 1996, AJ, 112, 146

This paper has been typeset from a T_EX/L^AT_EX file prepared by the author.